



Why does stratospheric aerosol forcing strongly cool the warm pool?

Moritz Günther¹, Hauke Schmidt¹, Claudia Timmreck¹, and Matthew Toohey²

¹Climate Physics, Max Planck Institute for Meteorology, Hamburg, Germany

²Institute of Space and Atmospheric Studies, University of Saskatchewan, Saskatoon, Saskatchewan, Canada

Correspondence: Moritz Günther (moritz.guenther@mpimet.mpg.de)

Received: 13 February 2024 – Discussion started: 20 February 2024

Revised: 4 April 2024 – Accepted: 4 April 2024 – Published: 24 June 2024

Abstract. Previous research has shown that stratospheric aerosol causes only a small temperature change per unit forcing because they produce stronger cooling in the tropical Indian Ocean and the western Pacific Ocean than in the global mean. The enhanced temperature change in this so-called “warm-pool” region activates strongly negative local and remote feedbacks, which dampen the global mean temperature response. This paper addresses the question of why stratospheric aerosol forcing affects warm-pool temperatures more strongly than CO₂ forcing, using idealized MPI-ESM simulations. We show that the aerosol’s enhanced effective forcing at the top of the atmosphere (TOA) over the warm pool contributes to the warm-pool-intensified temperature change but is not sufficient to explain the effect. Instead, the pattern of surface effective forcing, which is substantially different from the effective forcing at the TOA, is more closely linked to the temperature pattern. Independent of surface temperature changes, the aerosol heats the tropical stratosphere, accelerating the Brewer–Dobson circulation. The intensified Brewer–Dobson circulation exports additional energy from the tropics to the extratropics, which leads to a particularly strong negative forcing at the tropical surface. These results show how forced circulation changes can affect the climate response by altering the surface forcing pattern. Furthermore, they indicate that the established approach of diagnosing effective forcing at the TOA is useful for global means, but a surface perspective on the forcing must be adopted to understand the evolution of temperature patterns.

1 Introduction

Stratospheric sulfate aerosol forcing can arise naturally from volcanic eruptions or artificially from the deliberate injection of sulfur into the stratosphere. The aerosol increases the reflection of shortwave (SW) radiation, which constitutes a negative forcing and cools the Earth. The sulfate aerosol also absorbs near-infrared and terrestrial longwave (LW) radiation, causing a smaller positive forcing and radiative heating in the stratosphere. The radiative forcing from stratospheric aerosol produces a stronger feedback and, hence, a smaller temperature change per unit forcing than the radiative forcing from CO₂ (e.g., Hansen et al., 2005; Gregory et al., 2016; Zhao et al., 2021; Günther et al., 2022). The pronounced negative feedback to volcanic eruptions contributes to variations in Earth’s radiative feedback parameter over the historical period, where high volcanic activity coincides with

strong global-mean feedback (Gregory and Andrews, 2016; Gregory et al., 2020; Salvi et al., 2023).

Modeling studies have shown that the strong feedback to stratospheric aerosol forcing arises from enhanced changes in warm-pool (WP) temperatures relative to the global mean (Günther et al., 2022). The WP comprises the equatorial Indian Ocean and the western Pacific Ocean (30° S–30° N, 50° E–160° W) and is the main region of deep convection due to its high sea surface temperature (SST). The amplified temperature change in the WP increases the tropical to mid-latitude inversion strength and activates strong negative lapse rate and cloud feedbacks (Ceppi and Gregory, 2019). The cloud and lapse rate feedback processes that originate from the WP temperature change are powerful enough to impact the global-mean radiative feedback, which explains how the

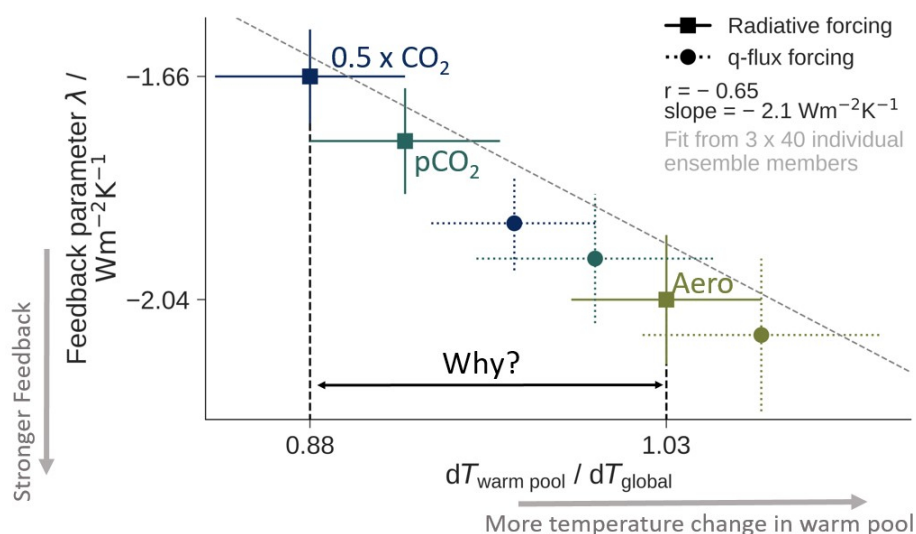


Figure 1. Relationship between the feedback parameter and the relative WP temperature change. The quantity on the x axis is a measure for how strongly the WP cools relatively to the global mean. The symbols indicate the mean, and the lines indicate the standard errors. Squares represent results from the radiatively forced simulations. Circles represent results from the q -flux-forced simulations which are discussed in Sect. 3.5. Stratospheric aerosol forcing (Aero) causes a stronger WP temperature change and, hence, a stronger feedback than $0.5 \times \text{CO}_2$ forcing. The dashed gray fit line is calculated from a regression through a total of 120 radiatively forced simulations, 40 for each forcing agent (see Sect. 2).

pronounced WP cooling from stratospheric aerosol can cause substantially more negative feedback than CO_2 forcing.

However, it has remained unclear why aerosol forcing impacts WP temperatures more strongly than CO_2 forcing, which constitutes the principal incentive for pursuing this study (see Fig. 1). We explore hypotheses that could explain the causes of the different temperature patterns.

The most obvious hypothesis is that the different top of the atmosphere (TOA) effective-forcing patterns cause the temperature pattern differences. Model studies have focused on the impact of aerosol from large tropical eruptions, which lead to aerosol optical depths that are largest in the low latitudes. Since both aerosol optical depth and incoming solar radiation peak in the tropics, they could combine to produce intensified low-latitude radiative forcing. In comparison, CO_2 forcing is relatively spatially uniform. The tropically enhanced forcing pattern from aerosols has been proposed to be the reason for the pronounced temperature changes in the tropics, in particular in the WP (Salvi et al., 2023; Günther et al., 2022).

Alternatively, the different temperature patterns of aerosol and CO_2 forcing could originate from other distinctive features of the forcing agents. It has been argued that spectral differences could play a role since aerosol forcing predominantly affects SW radiation, while CO_2 exclusively affects LW radiation (Joshi and Shine, 2003; Bony et al., 2006). Günther et al. (2022) also speculated about a fundamental difference in feedback strength in terms of positive vs. negative forcing; however, an extension of the ensemble analyzed in their study made this hypothesis less plausible.

Another essential discrepancy between aerosol and CO_2 forcing is the heating of the stratosphere and upper troposphere due to the aerosol's absorption of radiation. The diabatic heating leads to a cold-point warming, which allows more water vapor to enter the stratosphere (Joshi and Shine, 2003; Kroll et al., 2021), with potential impacts on the temperature response (Lee et al., 2023). The heating can furthermore alter the energy balance and the meridional temperature gradient in the upper troposphere and stratosphere. This has consequences for the strength and position of the polar vortex (e.g., Toohey et al., 2014; Azoulay et al., 2021; Bittner et al., 2016; Graf et al., 2007) and can lead to an acceleration of the Brewer–Dobson circulation (BDC), although different studies yield conflicting results (Garfinkel et al., 2017). Within the wave-driven BDC, air moves upwards in the tropical stratosphere. In the tropics, forced upwelling leads to an adiabatic cooling of the environment that depends on the vertical velocity and the temperature gradient (Birner and Charlesworth, 2017). The air then moves polewards and descends in the extratropical stratosphere, where it causes adiabatic heating (Holton et al., 1995). Changes in the BDC due to stratospheric aerosol forcing have been the subject of previous research (e.g., Garfinkel et al., 2017; SPARC, 2022; Diallo et al., 2017; Richter et al., 2017), but the consequences for radiative feedback and temperature patterns have not been explored yet.

Motivated by the temperature pattern's importance for radiative feedbacks, we investigate which of the distinctions between CO_2 and aerosol forcing cause the differences in the temperature change patterns, particularly with respect to the

WP. Using coupled climate model simulations, we present arguments that the pattern of TOA effective forcing is only weakly related to the pattern of surface temperatures and the radiative feedback. Instead, the surface forcing is more relevant for explaining the temperature pattern. We show that the contrast between adiabatic cooling in the tropical stratosphere and heating in the extratropical stratosphere from an accelerated BDC causes additional negative forcing at the tropical surface, which contributes to enhanced cooling of the tropics.

2 Simulations and methods

2.1 Model

We perform simulations with the climate model MPI-ESM 1.2 in the low-resolution setup (Mauritsen et al., 2019). The atmospheric component, ECHAM6 (Stevens et al., 2013), is resolved with $1.875^\circ \times 1.875^\circ$ at 47 levels. It is coupled to the ocean component, MPIOM (Jungclaus et al., 2013), which runs on a bipolar grid with a resolution of 1.5° near the Equator. MPI-ESM also includes modules for land processes and ocean biogeochemistry (Reick et al., 2021; Ilyina et al., 2013). Since no interactive atmospheric chemistry processes are included, aerosol and trace gases are prescribed with monthly climatological fields that represent unforced pre-industrial conditions.

2.2 Simulations

We perform simulations with three forcings: an abrupt halving of the CO_2 concentration ($0.5 \times \text{CO}_2$), an abrupt increase in the stratospheric aerosol concentration (Aero), and a patterned CO_2 simulation with spatially and seasonally varying CO_2 concentrations (pCO_2).

The Aero simulations are designed to represent the time-mean forcing induced by a strongly idealized tropical volcanic eruption or by deliberate stratospheric aerosol injection. We derive monthly and zonal mean fields of aerosol optical properties from the EVA forcing generator (Toohey et al., 2016) for one January and one July eruption, both with an injection mass of 20 Tg sulfur. The July eruption is then shifted by 6 months, and the average of both phase-matched eruptions is computed in order to remove seasonal transport asymmetries while preserving a realistic poleward mass transport. We prescribe the average of the first 3 post-eruption years as a time-invariant forcing to MPI-ESM. Constructing the aerosol forcing to be step-like in time allows for a consistent comparison to the $0.5 \times \text{CO}_2$ forcing. The aerosol is only coupled to the radiation, and it is not transported by the model, does not evolve in time, and does not interact directly with clouds or ozone. While these restrictions certainly limit realism, they allow us to isolate the effects of stratospheric aerosol in an idealized, interpretable frame-

work. The most important radiative properties of the aerosol input are shown in Fig. 2a.

In pCO_2 , CO_2 concentrations in each grid box and month are chosen such that they give rise to an effective TOA-forcing field which is approximately equal to the TOA radiative forcing of Aero in space and time. The rationale for this experiment's design is as follows: if the WP-enhanced TOA-forcing pattern of stratospheric aerosol is responsible for the WP-enhanced temperature pattern then the same effect should appear in a CO_2 -forced simulation with a WP-enhanced forcing pattern. The iterative process that was used to determine the CO_2 concentrations is described in Appendix A. The annual-mean input field of spatially varying CO_2 concentrations is shown in Fig. 2b. The CO_2 concentrations are lowest over the WP and are slightly higher than the pre-industrial value over the poles. The resulting field of effective forcing shares these broad features and is shown in Fig. 3a.

To test the hypothesis that the effective-forcing pattern from stratospheric aerosol causes the enhanced WP temperature change, we perform the three sets of simulations summarized in Table 1.

2.2.1 Coupled simulations with radiative forcing

From a 1000-year control simulation with pre-industrial conditions (piControl), we branch one simulation for each forcing ($0.5 \times \text{CO}_2$, Aero, pCO_2) every 25 years, leading to a total of 3×40 ensemble members, each run for 10 years.

2.2.2 Simulations with fixed SST and sea ice

As an analog to the coupled simulations, for each forcing, we perform one 100-year simulation with SST and sea ice concentrations fixed to climatological control values. By subtracting the mean climate state in these perturbed simulations from the model's mean control climate state (piClim-control), we can diagnose effective forcing at the TOA and at the surface as well as adjustments (Forster et al., 2016; Sherwood et al., 2015). Results from the fixed-SST simulations are averaged over all 100 simulated years except the first to allow for rapid adjustments. Forster et al. (2016) recommend 30 years to reliably diagnose the global mean effective forcing. We find that 100 years are necessary to determine the spatial pattern of the effective forcing, especially at the surface, where interannual variability is strong.

In addition to the fixed-SST simulation with the Aero forcing, we perform a simulation with non-absorbing aerosol forcing and only with fixed SST and sea ice in order to isolate the effects that arise from the stratospheric heating, particularly the acceleration of the BDC (Sect. 3.3). For this simulation, we take the forcing from Aero but set the single scattering albedo (ratio of scattering to total extinction) to 1 everywhere. The total extinction is then multiplied by $(1 - \text{initial single scattering albedo})$ in order to avoid increases in the

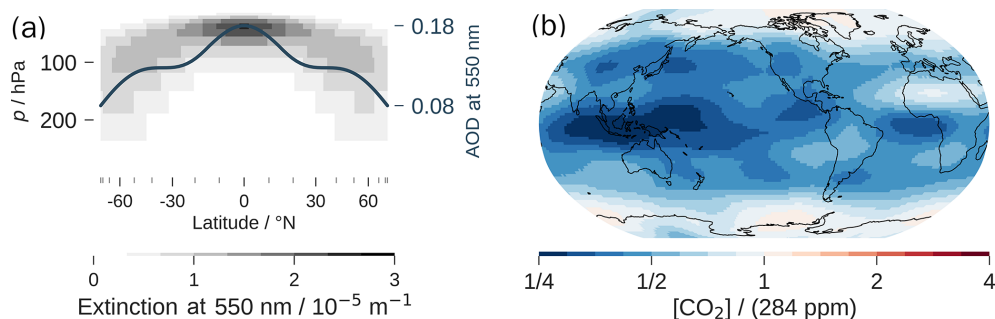


Figure 2. Forcing input for the simulations. **(a)** Aerosol radiative properties that serve as input for the Aero simulation: extinction as a function of latitude and pressure and aerosol optical depth (AOD, vertically integrated extinction) as function of latitude, computed with EVA (Toohey et al., 2016). **(b)** Annual-mean field of CO_2 concentrations (in units of the pre-industrial CO_2 concentration) that serves as input for the p CO_2 simulation. In the actual simulation, monthly varying fields are used (Figs. A1 and A2 in the Appendix). The fields were computed with the algorithm described in Appendix A.

reflectivity. For slightly different approaches to isolate the stratospheric heating effects, see Simpson et al. (2019) and Wunderlin et al. (2024). The focus of this study will be on the absorbing aerosol forcing (Aero).

2.2.3 Coupled simulations with q -flux forcing

Forcing the climate system not radiatively but with a “ghost forcing” (Hansen et al., 1997) at the surface allows for an examination of the way the surface forcing pattern affects the temperature pattern without any perturbations to the atmosphere’s radiative properties. We derive the surface effective forcing from the fixed-SST simulations as the difference between all surface fluxes (radiative and turbulent) of the perturbed simulations and piClim-control. We then prescribe these flux anomalies as an additional heat source or sink (q flux) to the ocean and compute an ensemble of 40 simulations for each forcing agent, where each simulation lasts for 10 years. Note that the atmosphere is still fully coupled to the dynamical ocean.

2.3 CMIP6 output

We complement the dedicated MPI-ESM simulations with the output of the piControl and historical simulations from phase 6 of the Coupled Model Intercomparison Project (CMIP6; Eyring et al., 2016) to test the results using other models. We include all 23 models that provide the necessary output to compute adiabatic cooling in the stratosphere according to Eq. (2) (see Sect. 2.4.4). For models with multiple realizations, the ensemble-mean is calculated after applying Eq. (2) so that each model is weighted equally. A list of all models and the number of ensemble members can be found in Table D1 in the Appendix.

2.4 Defining forcing, feedback, WP enhancement, and adiabatic cooling

2.4.1 Effective forcing

Effective forcing is defined as the time-mean flux change in a perturbed simulation compared to an unperturbed control simulation, both with the same prescribed SST and sea ice (Forster et al., 2016). It is traditionally measured at the TOA, where it consists of SW and LW flux changes. We also diagnose effective forcing at the surface, where, additionally, the sensible and latent heat fluxes must be taken into account.

2.4.2 Feedback parameter

We employ the definition of the “differential feedback parameter” of Rugenstein and Armour (2021), namely $\lambda = \frac{\partial N}{\partial T}$, with global-mean TOA flux N and global-mean near-surface air temperature T , obtained by regression over 10 years. The differential feedback parameter characterizes the transient response to the forcing on a timescale of 10 years and bears only very limited implications for the long-term or equilibrium response.

2.4.3 Warm-pool index (WPI)

Given the elevated role of the WP, spatial patterns can be meaningfully measured with a simple WP index (WPI), which indicates how strongly a quantity is concentrated in the WP. For patterns of effective forcing F , we define it as $\text{WPI}_F = F_{\text{WP}}/F_{\text{global}}$. Temperatures vary with time; thus, for patterns of temperature change T , we define $\text{WPI}_T = dT_{\text{WP}}/dT_{\text{global}}$, obtained by regression over 10 years. Values greater than 1 indicate greater forcing or temperature change in the WP than in the global mean.

Table 1. Overview of the MPI-ESM simulations.

	0.5 × CO ₂	Aero	pCO ₂	Aero (non-absorbing)
Coupled: radiative forcing	40 × 10 years	40 × 10 years	40 × 10 years	—
Fixed SST: radiative forcing	100 years	100 years	100 years	100 years
Coupled: <i>q</i> -flux forcing	40 × 10 years	40 × 10 years	40 × 10 years	—

2.4.4 Adiabatic cooling in the stratosphere

Upwelling in the tropical stratosphere causes adiabatic cooling at rate K (in Ks^{-1}), which is proportional to the residual mean vertical velocity \bar{w}^* and the deviation of the temperature profile $\frac{\partial T}{\partial z}$ from a dry adiabat $-\frac{g}{c_p}$ (Birner and Charlesworth, 2017):

$$K = -\bar{w}^* \left(\frac{\partial T}{\partial z} + \frac{g}{c_p} \right), \quad (1)$$

with the specific heat capacity of dry air c_p and gravitational acceleration g . The residual mean vertical velocity \bar{w}^* is obtained from a transformed Eulerian mean analysis (e.g., Butchart, 2014). \bar{w}^* combines the mass flux contributions from the mean velocity w and the eddies (Butchart, 2014) and therefore better represents the mass flux than w alone. Using the hydrostatic approximation $\rho dz = -dp/g$, we calculate the integrated adiabatic cooling of the stratosphere as the power flux density Q_{adi} (in Wm^{-2}) according to

$$Q_{\text{adi}} = c_p \int_{\text{strat.}} K(z) \rho(z) dz = -\frac{c_p}{g} \int_{100 \text{ hPa}}^{1 \text{ hPa}} K(p) dp. \quad (2)$$

By vertically integrating over the stratosphere, we effectively treat it as one layer that causes adiabatic cooling. Changing the lower limit to 70 hPa changes the numbers by up to 25 % but not in a way that would affect the conclusions.

The changes in K can be decomposed linearly into contributions from changes in \bar{w}^* and $\frac{\partial T}{\partial z}$:

$$\Delta_{\bar{w}^*} K = \frac{\partial K}{\partial \bar{w}^*} \Big|_0 \Delta \bar{w}^* = - \left(\frac{\partial T}{\partial z} \Big|_0 + \frac{g}{c_p} \right) \Delta \bar{w}^*, \quad (3)$$

$$\Delta_{\frac{\partial T}{\partial z}} K = \frac{\partial K}{\partial \frac{\partial T}{\partial z}} \Big|_0 \Delta \frac{\partial T}{\partial z} = -\bar{w}^* \Big|_0 \Delta \frac{\partial T}{\partial z}. \quad (4)$$

The notation $|_0$ indicates values in the unperturbed state, i.e., from the piClim-control or piControl simulation. Plugging these cooling rates into Eq. (2) yields the adiabatic-cooling changes ΔQ_{adi} due to changes in \bar{w}^* and $\frac{\partial T}{\partial z}$.

3 Results

3.1 Effects of the TOA-forcing pattern on the temperature change pattern

First, we explore the hypothesis that the WP-enhanced forcing pattern from volcanic aerosol causes the WP-enhanced

temperature response. The TOA effective-forcing fields of the radiatively forced simulations are shown in Fig. 3a. All fields average globally to approximately -3.5 Wm^{-2} but exhibit different patterns. Compared to the relatively uniform $0.5 \times \text{CO}_2$ TOA effective-forcing pattern, Aero exhibits a pronounced forcing pattern. The TOA forcing of Aero is 1.5 Wm^{-2} more negative in the WP than in the global mean, mainly due to three effects (Fig. C1 in the Appendix): first, a stronger instantaneous forcing in the tropics than in the extratropics due to higher aerosol concentration and insolation (-1 Wm^{-2}); second, a weaker LW effect over the WP than over the entirety of the tropics (-0.2 Wm^{-2}) due to the LW effect being weaker over high clouds than over low clouds or the surface; third, more negative SW cloud adjustments over the WP than over the entirety of the tropics (-0.3 Wm^{-2}). The last point may be model-dependent and differs from Marshall et al. (2020), who find strong positive SW cloud adjustments in UK-ESM.

By design, the pCO₂ TOA-forcing field shares the Aero forcing field's main features, although it is slightly less enhanced over the WP, which we will address later. The TOA effective-forcing fields of Aero and pCO₂ agree well – not only in terms of the annual mean but also in each month (Figs. A1 and A2 in the Appendix).

The temperature change patterns of all coupled 10-year simulations are broadly similar (Fig. 3b). Temperature change is amplified in the Arctic; moderate in low latitudes, including the WP; and suppressed over the Southern Ocean. The most relevant region for the feedback is the WP, where small differences have substantial impacts on the global feedback, with changes of roughly $-0.2 \text{ Wm}^{-2} \text{K}^{-1}$ per 0.1 WPI_T points in MPI-ESM (Fig. 1). The definition $\text{WPI}_T = dT_{\text{WP}}/dT_{\text{global}}$ is equivalent to the WP average of the temperature pattern shown in the black box in Fig. 3b. Despite the fact that the temperature pattern differences among the simulations over the WP are relatively small compared to those in other regions, these small changes dominate the global mean radiative feedback parameter (Dong et al., 2019; Günther et al., 2022).

Although Aero and pCO₂ are almost equally strongly forced in the WP, the WPI_T of the temperature pattern of pCO₂ (0.92) is smaller than that of Aero (1.03). We perform Student's *t* tests on the distributions of WPI_T from the 40 ensemble members of each forcing agent under the null hypothesis that they are drawn from distributions with the same average. While the WPI_T values of $0.5 \times \text{CO}_2$ and pCO₂ are not sig-

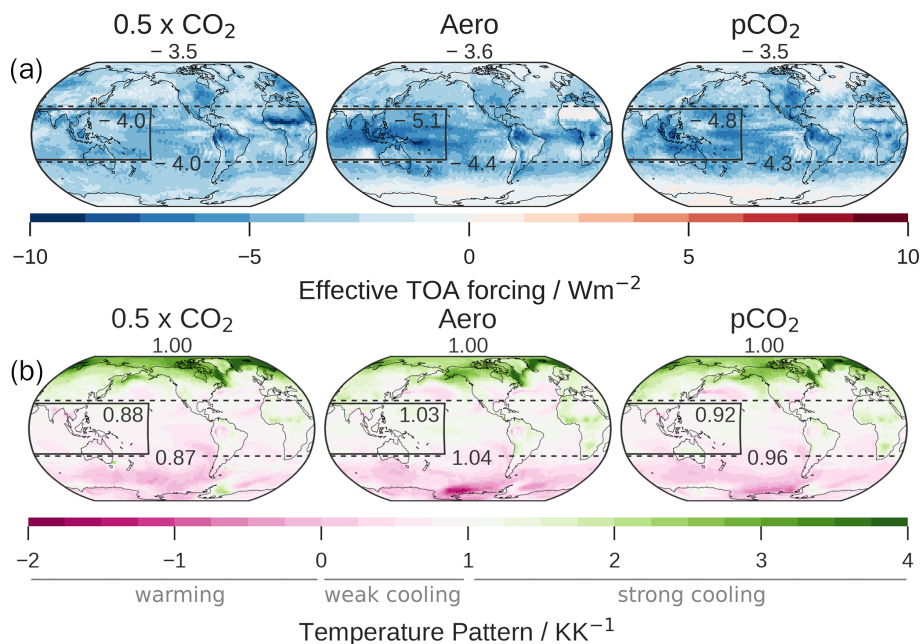


Figure 3. (a) Annual-mean TOA effective forcing obtained from the difference between the forced simulations with fixed SST and the control simulation with fixed SST. (b) Ensemble-mean 2 m temperature change patterns (ratio of local to global mean temperature change) of the radiatively forced coupled simulations. Values greater than 1 (green) indicate cooling stronger than the global average, while values lower than 1 (pink) indicate cooling that is weaker than average. Values lower than zero indicate warming. The WP and tropics are shown with solid and dashed lines, and the field average over each region is shown in the respective box. The global mean is shown at the top of each panel. Standard errors are negligible compared to the shown precision in (a). In (b), standard errors of the means over the WP and the tropics are ≈ 0.04 – 0.05 KK^{-1} .

nificantly different ($p = 0.2$), the WPI_T values of Aero and pCO_2 are distinct ($p = 10^{-6}$). Although the TOA-forcing patterns of pCO_2 and Aero are similar, their temperature change patterns are not when measured by WPI_T (Fig. 1). This contradicts the hypothesis that the WP-enhanced TOA-forcing pattern of Aero causes the WP-enhanced temperature change pattern. If that were the case, the WP should cool equally strongly in Aero and pCO_2 .

This result is limited by the fact that the forcing pattern of pCO_2 is not quite as WP-enhanced as in Aero: the WPI_F (WP forcing divided by global mean forcing) is only 1.36 in pCO_2 but is 1.44 in Aero. However, even when applying a correction factor of $1.44/1.36$ to the WPI_T values of pCO_2 , the WPI_T values remain significantly different from Aero, albeit with a higher p value ($p = 0.02$).

In summary, the pCO_2 simulation with a TOA-forcing pattern almost as WP-heavy as Aero does not produce a temperature change pattern as WP-heavy as Aero. Instead, its temperature change pattern is rather similar to the $0.5 \times \text{CO}_2$ simulation (see also Fig. 1). Hence, we arrive at the conclusion that another process which is specific to aerosol forcing must cause the temperature pattern differences.

3.2 Surface forcing pattern

The rationale of the TOA-forcing hypothesis was that stronger forcing in the WP could lead to stronger temperature change in the WP. However, the ocean does not directly respond to the forcing at the TOA but rather responds directly to the forcing at the surface, which might therefore be more relevant. In the following section, we examine the surface effective forcing and how it differs from the TOA effective forcing.

There are multiple constraints to surface forcing: the land and atmosphere have small heat capacities and therefore cannot act as energy reservoirs on timescales of the 100-year fixed-SST simulation. If there were substantial fluxes into the atmosphere or the land, they would heat up or cool down until the fluxes become zero. The timescale of these adjustments is fast due to the small heat capacities of the land and atmosphere. Only the ocean (due to its fixed SST) and the TOA can support non-zero fluxes in the steady state of the fixed-SST simulations. These considerations imply that the surface effective forcing over land must be zero. The fact that the global-mean flux into the atmosphere is zero implies that the global-mean effective forcings at the TOA and the surface must be equal (see also Eq. 5).

Figure 4 shows the annual-mean effective radiative forcing at the TOA and the surface, as well as their difference,

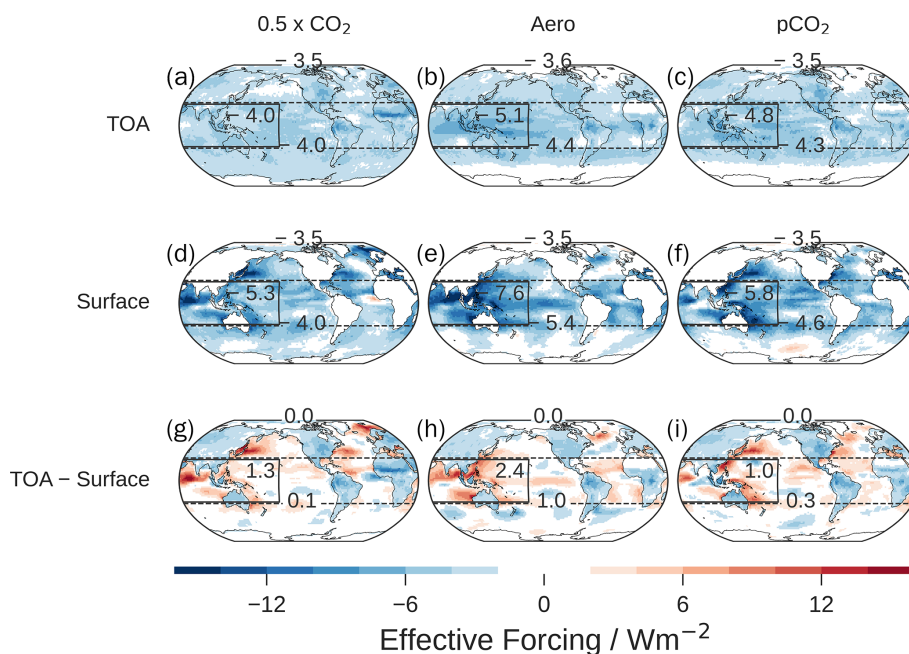


Figure 4. Effective forcing of the radiatively forced simulations at the TOA (a, b, c) and at the surface (d, e, f) and their difference (g, h, i). The difference between TOA and surface effective forcing is the effective forcing on the atmosphere, and this can be interpreted as a redistribution of negative forcing from blue to red regions when going from the TOA to the surface. The WP and tropics are shown with solid and dashed lines, and the field average over each region is shown in the respective box. The global mean is shown at the top of each panel. The standard errors are generally negligible compared to the shown precision, except for the WP mean of the surface and TOA–surface ($\approx 0.2 \text{ Wm}^{-2}$) and the tropical mean of the surface and TOA–surface ($\approx 0.1 \text{ Wm}^{-2}$).

diagnosed from the fixed-SST simulations. The surface forcing exhibits a richer spatial structure than the TOA forcing. Furthermore, the WP intensification of the forcing in Aero is much more pronounced at the surface than at the TOA: at the WP surface, it is more than twice as strong as in the global mean. In comparison, the surface forcing in pCO₂ is only slightly more WP-enhanced than in $0.5 \times \text{CO}_2$.

The difference between the TOA and surface forcing is the effective forcing that acts on the atmosphere, which is zero in the global mean but has a pattern. It must be locally balanced by changes in the horizontal heat flux divergence Q since the atmosphere has no relevant sinks or sources of energy on long timescales.

$$F_{\text{TOA}} - F_{\text{surface}} = F_{\text{atm}} \quad (5)$$

$$F_{\text{atm}} + Q = 0 \quad (6)$$

F_{TOA} and F_{surface} denote the effective forcing at the TOA or at the surface, respectively. F_{atm} denotes the effective forcing on the atmosphere. All effective-forcing fields are a function of longitude and latitude. Both sides of Eq. (5) can be globally averaged to zero.

The forcing on the atmosphere equals the change in the horizontal atmospheric heat flux divergence at fixed SST. Considering the perspective from the TOA looking down to the surface, the atmosphere shifts the negative forcing from grid points with negative values towards grid points with

positive values. The negative forcing is redistributed from columns over land to columns over ocean in all simulations (Fig. 4, bottom row). This effect arises somewhat artificially from the fact that effective forcing is diagnosed at fixed SST concentrations and sea ice concentrations but not fixed land temperatures. In Aero, there is an additional convergence of negative forcing at the WP surface ($2.4 \pm 0.2 \text{ Wm}^{-2}$ compared to $1.0 \pm 0.2 \text{ Wm}^{-2}$ in pCO₂ and $1.3 \pm 0.2 \text{ Wm}^{-2}$ in $0.5 \times \text{CO}_2$).

We argue that the surface forcing is the critical factor that distinguishes aerosol from CO₂ forcing. The differences between the TOA and surface forcing are imposed by heat transport changes that arise from anomalous circulations. They come about as adjustments which are specific to the forcing agent. We hypothesize that the WP surface in Aero is so strongly forced because the anomalous atmospheric circulation leads to an anomalous energy transport out of the WP or, equivalently, moves positive forcing away from the WP surface. In the following sections, we aim to (1) explain how the differences in atmospheric-forcing divergence arise from the circulation changes and (2) determine if these differences cause the distinctions among the temperature change patterns.

3.3 Explaining the atmospheric-forcing divergence

What explains the different structures of the forcing on the atmosphere (bottom row of Fig. 4)? Most of the spatial structure arises from variations in the latent heat flux at the surface (not shown). Therefore, it is mostly the latent heat flux that reacts to energetic constraints from the atmosphere, consistently with previous studies (Fajber and Kushner, 2021; Fajber et al., 2023). However, this does not explain why the atmosphere redistributes energy and which circulations accomplish this energy transport.

Equation (6) states that the forcing on the atmosphere is balanced by heat transport. We focus on the anomalous energy export out of the WP and on the question of why this anomaly is stronger for Aero. To this end, we partition the energy export into a meridional component, i.e., the energy transport from the tropics to the extratropics, and a tropical–zonal component, i.e., the transport from the WP to tropical non-WP regions. In the TOA–surface row of Fig. 4, the meridional energy transport is equal to the average over the tropics ($1.0 \pm 0.1 \text{ Wm}^{-2}$ in Aero compared to $0.1 \pm 0.1 \text{ Wm}^{-2}$ in $0.5 \times \text{CO}_2$), and the zonal energy transport is measured by the difference between the WP mean and the tropical mean ($1.4 \pm 0.2 \text{ Wm}^{-2}$ in Aero compared to $1.2 \pm 0.3 \text{ Wm}^{-2}$ in $0.5 \times \text{CO}_2$).

Obvious explanations for these transports could be changes in gross moist stability, the Hadley or Walker circulations, or eddy energy fluxes. Indeed, the tropical tropospheric zonal overturning circulation has been shown to weaken as a consequence of stratospheric heating (Ferraro et al., 2014; Simpson et al., 2019). However, a weaker zonal overturning circulation cannot be the reason for increased energy flux out of the WP unless it is overcompensated for by increases in gross moist stability. We argue that the circulation changes associated with the atmospheric energy budget do not project onto the Hadley and Walker circulations. Instead, the meridional transport is accomplished via the BDC, and the tropical–zonal transport arises from an anomalous ocean–land circulation. This only applies to the direct circulation adjustments, and we do not make any statement about temperature-dependent changes to the Hadley or the Walker circulations from stratospheric aerosol forcing. The meridional and tropical–zonal components will be treated separately in the following.

3.3.1 Meridional energy transport: adiabatic cooling from the Brewer–Dobson circulation

We propose that the meridional transport of energy from the tropics to the extratropics arises from increased adiabatic cooling in the tropics via the BDC. Stratospheric aerosol causes a meridional heating gradient in the stratosphere, which affects the wave propagation and therefore the wave driving of the BDC (Garcia and Randel, 2008). An increase in adiabatic cooling could arise from an acceleration of the

vertical velocity (i.e., the BDC) or an increase in the vertical temperature gradient (see Eq. 1). The changes in adiabatic cooling in the fixed-SST simulations compared to piClim-control, calculated according to Eq. (2), are shown in Table 2. In the tropics, the BDC causes an additional adiabatic cooling of 0.9 Wm^{-2} in Aero, 0.0 Wm^{-2} in $0.5 \times \text{CO}_2$, and 0.1 Wm^{-2} in pCO₂. In Aero, most of this is driven by changes in the upwelling speed, and only a small part is due to changes in the stratospheric lapse rate. While the upwelling speed influences the adiabatic cooling proportionally according to Eq. (2), changes in the temperature profile influence adiabatic cooling only in so far as they change the difference between the actual lapse rate and the dry adiabatic lapse rate. Since this difference is already quite large in the unperturbed stratosphere (10 K km^{-1} dry adiabatic lapse rate vs. -2 K km^{-1} stratospheric lapse rate), moderate changes in the stratospheric lapse rate will only have a small effect on the adiabatic cooling. However, eventually, all changes in adiabatic cooling are driven by changes in the global stratospheric temperature distribution, as the differential heating between the Equator and the poles affects wave propagation and, therefore, the speed of the BDC (Garcia and Randel, 2008). A measure for the BDC strength is the tropically averaged residual mean vertical velocity \bar{w}^* , which increases in Aero by $10 \pm 2\%$ at 70 hPa and by $24 \pm 2\%$ at 30 hPa. In the CO₂-forced simulations, these changes are on the order of the uncertainty.

Adiabatic cooling is not a sink of energy in the global energy budget. The energy is released during the sinking motion in the extratropics and, therefore, constitutes an energy transport from the tropics to the extratropics (Richter et al., 2017). The mechanism of energy export due to the BDC explains the meridional energy transport of slightly less than 1 Wm^{-2} from the tropics to extratropics seen in Fig. 4h. The forcing anomalies are communicated from the stratosphere to the tropical tropopause layer and the free troposphere via radiation and are then passed on via convection to the surface.

We turn to the additional simulation with fixed SST and a prescribed aerosol forcing similar to Aero, where the aerosol is modified to only scatter but not absorb radiation. This precludes the aerosol from heating the stratosphere, which should, in turn, prevent the BDC mechanism. Consistently with our expectations, we find no anomalous energy transport from the tropics to the extratropics (Table 2).

Note that an increase in adiabatic cooling does not imply that the tropical stratosphere becomes colder – it just warms less than it would if there was no acceleration of the BDC. The stratosphere heats in Aero and the CO₂-forced simulations, leading to a small additional adiabatic cooling from the increased lapse rate. However, only in Aero does the BDC accelerate considerably, which provides the bulk of the adiabatic-cooling effect.

Table 2. Anomalous adiabatic cooling in the stratosphere calculated according to Eq. (2) and averaged over the tropics (30° N to 30° S). Negative values represent cooling. Standard errors are only shown where they are at least on the order of the precision shown, i.e., $O(0.1 \text{ Wm}^{-2})$. The lower rows show the contributions from changes in the upwelling speed and the lapse rate, respectively.

	$0.5 \times \text{CO}_2$	Aero	pCO ₂	Aero (non-absorbing)
$\Delta Q_{\text{adi}} (\text{Wm}^{-2})$	0.0	−0.9	−0.1 ± 0.1	0.0
ΔQ_{adi} due to $\Delta \bar{w}^*$ (Wm^{-2})	0.2	−0.7	0.1 ± 0.1	0.0
ΔQ_{adi} due to $\Delta \partial T / \partial z$ (Wm^{-2})	−0.2	−0.2	−0.2	0.0

3.3.2 Tropical–zonal energy transport: ocean-to-land circulation

All simulations exhibit a zonal energy transport from the WP to the tropical non-WP regions. This tropical–zonal energy transport is not a big contributor to the differences between the Aero and $0.5 \times \text{CO}_2$ forcing patterns and is, therefore, not a focus of our study. Nevertheless, we briefly lay out the reasons for this anomalous circulation. The explanations are somewhat rooted in the way forcing is diagnosed in models and only partially apply to the real world.

Since land temperatures vary freely in the fixed-SST simulations, the land cools down rapidly, which leads to an enhanced energy flux from the atmosphere to the land. For the atmospheric energy budget to be closed, this energy must be replenished from the ocean, which can draw from an infinite energy reservoir due to the fixed-SST ocean surface. Consequentially, an anomalous energy transport arises from the ocean towards land (see Fig. B1 in the Appendix and the accompanying text). This is accomplished by land-to-ocean winds at the surface and ocean-to-land winds aloft, the latter of which also constitutes the directions of the energy flow. Since deep convection is impeded over non-WP regions, the anomalous circulation predominantly transports energy from WP ocean regions to the tropical land regions. For this reason, there is an additional energy export from the WP to the non-WP regions in all fixed-SST simulations.

Previous studies have noted the importance of land–ocean temperature contrasts and a resulting monsoon-like circulation in the fast response to abrupt forcing (Modak et al., 2016; Heede et al., 2020). While this circulation arises artificially in our fixed-SST simulations from the fact that land temperatures are not fixed, it would appear similarly in reality because land reacts much faster than ocean. This effect is important on a timescale of several months (Modak et al., 2016), which is comparable to the timescale of volcanic aerosol forcing. Our simulations show that this circulation causes an energy export out of the WP and might therefore contribute to a strengthening of the feedback to volcanic eruptions simply due to the timescale they act on. For long-term forcing such as anthropogenic greenhouse gases and solar radiation management, this effect would be less important. This raises the question of how the different timescales of volcanic aerosol and CO₂ forcing affect the feedback.

Further explanations and a figure showing the anomalous circulation can be found in Appendix B.

3.3.3 Sum of meridional and zonal terms

In total, the atmosphere exports 1.3 Wm^{-2} out of the WP in the $0.5 \times \text{CO}_2$ simulation but 2.4 Wm^{-2} in Aero, which leads to enhanced negative forcing at the WP surface in Aero (Fig. 4). In Aero, the atmosphere absorbs 0.9 Wm^{-2} of positive forcing in the tropics and exports it to the extratropics via the BDC (Table 2). The energy transport via the BDC explains most of the meridional energy transport and the difference between the surface forcing in the Aero and $0.5 \times \text{CO}_2$ experiments. The cooling of the land surface causes an additional zonal transport of energy from the WP ocean to tropical land regions via the free troposphere in all simulations. While the anomalous meridional transport via the BDC does not show substantial year-to-year variation, the zonal energy transport varies substantially interannually. Even using 100 years of fixed-SST simulations, its standard error (standard deviation in time divided by square root of sample size) is on the order of 10 % to 15 %, which is 1 order of magnitude higher than the standard error of the meridional transport. This implies the existence of substantial interannual variability, which originates from the atmosphere alone. Furthermore, the tropical–zonal energy transports of Aero and $0.5 \times \text{CO}_2$ differ only within 1 standard error and arise at least partly from the specifics of fixed-SST simulations, where temperatures are only prescribed at the ocean surface but not at the land surface. We therefore emphasize the BDC changes as the more important result and recommend caution in the interpretation of the zonal energy transport. In the following, we examine the forcing patterns and the meridional energy transport mechanism in CMIP6 models.

3.4 Testing the energy export mechanism with CMIP6 models

Salvi et al. (2023) provide an analysis of CMIP6 forcing patterns at the TOA and the surface (see their Fig. 10). For aerosol forcing from the Krakatau and Pinatubo eruptions, they find enhanced forcing in the tropics at the TOA and at the surface. However, while the WP enhancement of aerosol forcing at the surface is clearly visible, it is not substantially stronger than in the case of greenhouse gas forcing. This calls

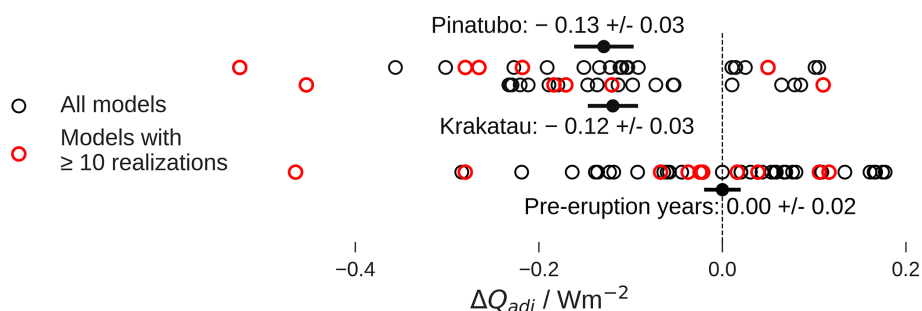


Figure 5. Tropical mean changes in stratospheric adiabatic cooling in the CMIP6 historical simulations in the pre-eruption (1882 and 1990) and post-eruption years (1884 and 1992) of Krakatau and Pinatubo, respectively, compared to the piControl simulations. The value from each model is shown by a circle. The green circles are from the five models with at least 10 realizations. Together, these models account for 80 % of all realizations. All values are calculated using Eq. (2). The error bars show the multi-model mean and standard error. Negative values indicate increased adiabatic cooling.

into question the existence of the BDC mechanism in CMIP6 models.

We explicitly test if the energy export due to the BDC increases after volcanic eruptions. A total of 23 models provide the necessary output to compute the adiabatic cooling in the historical coupled simulations. We compute the changes in the adiabatic cooling in the tropics according to Eq. (2) for the first post-eruption year of the Krakatau and Pinatubo eruptions (1884 and 1992, respectively). Since we restrict the computations to the tropics, where the eddy contribution is small, we simplify the analysis by using w instead of \bar{w}^* for the CMIP6 analysis. In MPI-ESM, this leads to an underestimate of the additional adiabatic cooling from aerosol forcing of approximately 10 %.

Most CMIP6 models show a moderate increase in adiabatic cooling, with multi-model averages of 0.12 and 0.13 Wm^{-2} for the Krakatau and Pinatubo eruptions, respectively (Fig. 5). The multi-model mean \pm standard error does not overlap with zero, indicating the presence of a significant effect. The 20 % to 80 % intervals are $[-0.22, -0.01]$ for Krakatau, $[-0.25, 0.01]$ for Pinatubo, and $[-0.11, 0.05]$ for the pre-eruption years. The adiabatic cooling in the pre-eruption years (1882 and 1990) is indistinguishable from the control simulation, which implies that the additional adiabatic cooling in the post-eruption years is indeed caused by the eruption and not some other historical forcing agent.

The effect is smaller than what we find in the fixed-SST simulations of MPI-ESM: assuming a peak global mean effective forcing from Krakatau and Pinatubo of approximately 1.8 Wm^{-2} (Salvi et al., 2023), the BDC cools the tropics by about 7 % of the global mean forcing in CMIP6 compared to about 25 % in our simulations. This difference is diminished when only taking into account the models with at least 10 realizations, where the influence of internal variability is reduced. In these models, the transport from the BDC is -0.16 $[-0.24, -0.07]$ Wm^{-2} for Krakatau and -0.25 $[-0.33, -0.16]$ Wm^{-2} for Pinatubo, corresponding to roughly 9 % and 14 % of the global mean forcing, respec-

tively. Apart from model differences, the remaining disparity between our results and the CMIP6 results could arise for three systematic reasons: first, using w instead of \bar{w}^* leads to a small underestimation. Second, the aerosol is short-lived, and not all of the post-eruption years are equally strongly affected by the presence of the aerosol. Third, the CMIP6 estimate is likely to be biased low because the historical coupled simulations cool in the post-eruption year, and there is a positive correlation between temperatures and the strength of the BDC (Garfinkel et al., 2017). The last point does not compromise our finding that the BDC reshapes the surface forcing pattern since the forcing is defined at zero surface temperature change.

In agreement with our CMIP6 analysis, model studies consistently show an acceleration of the BDC after volcanic eruptions (Garfinkel et al., 2017; Garcia et al., 2011; Pitari and Rizi, 1993; Pitari and Mancini, 2002; Aquila et al., 2013; Toohey et al., 2014; Muthers et al., 2016). In contrast, studies using reanalysis or observations provide mixed results. Some studies find enhanced wave activity in at least one hemisphere (Graf et al., 2007; Schnadt Poberaj et al., 2011), while others do not find stratospheric circulation changes after volcanic eruptions (Diallo et al., 2012; Seviour et al., 2012; SPARC, 2022). Since reanalysis products do not assimilate aerosol data and are hence ignorant to the ensuing heating rate anomalies in the stratosphere, they might not be a suitable tool to study the links between stratospheric heating and the BDC (Abalos et al., 2015). The absence of the upwelling effect in observational records might also be related to the choice of the metric: Toohey et al. (2014) argue that the upwelling change might be most pronounced in the middle and upper stratosphere, while observational studies focus on upwelling in the lower stratosphere.

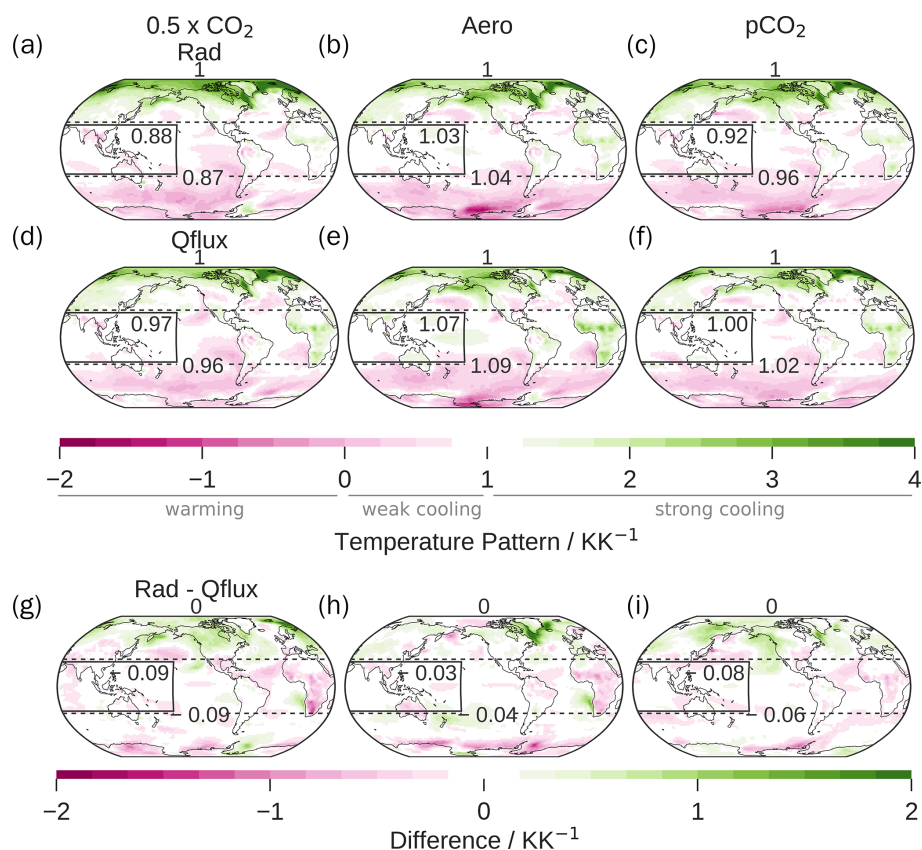


Figure 6. Ensemble-mean 2 m temperature change patterns (ratio of local to global mean temperature change) of the radiatively forced simulations (a–c) and the q -flux-forced simulations (d–f), as well as their difference (g–i). In panels (a) to (f), values greater than 1 (green) indicate cooling that is stronger than the global average, while values lower than 1 (pink) indicate cooling that is weaker than average. Values lower than zero indicate warming. In (a)–(f), the standard errors of the means over the WP and the tropics are ≈ 0.04 – 0.05 KK^{-1} . For the differences (g–i), the standard errors are $\approx 0.07 \text{ KK}^{-1}$.

3.5 Does the surface forcing pattern cause the surface temperature pattern?

If the previously demonstrated differences in the surface forcing cause the temperature pattern differences then these differences should appear in surface-forced simulations without any changes in aerosol or CO_2 concentrations. While this seems intuitive, it is not straightforward that stronger surface forcing in the WP causes stronger temperature changes in the WP. Results from q -flux Green's functions have shown that the temperature response to a localized surface flux is typically non-local (Lin et al., 2021; Liu et al., 2018a, b, 2022). We use the q -flux simulations to establish the link between local forcing and local temperature change in the WP. They are forced by a surface heat sink or source, each of them with a global mean of -3.5 Wm^{-2} , but with the patterns being diagnosed from the fixed-SST simulations (Fig. 4d–f).

Results from the q -flux simulations in terms of the temperature pattern and feedback are shown in Fig. 1. The simulations with more strongly concentrated surface forcing in the WP also cause stronger temperature changes in the WP

(Aero > pCO_2 > $0.5 \times \text{CO}_2$). These results support our hypothesis that stronger surface forcing in the WP leads to stronger surface temperature change in the WP. However, the temperature patterns differ between the q -flux-forced simulations and the corresponding radiatively forced simulations (Fig. 6), particularly with respect to temperature changes in the WP and the tropics. All q -flux-forced simulations cool more strongly in the WP and in the tropics than their radiatively forced counterparts. Generally, the pattern differences between radiatively and q -flux-forced simulations of the same forcing agent are on the same order of magnitude as the differences among the forcing agents. Possible reasons for these deviations are (i) the lack of changes in the atmospheric CO_2 concentrations and/or aerosol load, which affects the vertical structure of the atmosphere and the general circulation; (ii) the lack of forcing over land; (iii) the fact that we only include heat fluxes and no momentum or freshwater fluxes to force the ocean surface. Aquaplanet simulations show little difference between radiatively forced and q -flux-forced simulations (Haugstad et al., 2017), rendering hypothesis (i) – the absence of CO_2 and/or aerosol in the atmosphere

– as a cause for the differences unlikely. On the other hand, both CO₂-forced simulations show a more positive PDO (Pacific Decadal Oscillation)-like temperature change pattern in the radiatively forced simulations compared to the q -flux-forced simulations, which could be an indication that this part of the temperature pattern is due to the direct effect of CO₂. In CESM2 simulations with historical forcing, the absence of wind stress forcing causes statistically significant changes in the SST pattern (McMonigal et al., 2023) towards a more WP-enhanced temperature pattern, consistent with the bias in our simulations and with hypothesis (iii), the momentum-forcing hypothesis.

The exact causes are beyond the scope of this study and warrant further research. Despite the shortcomings, we interpret the results from the q -flux-forced simulations to support our hypothesis that strong surface forcing in the WP leads to strong surface cooling in the WP.

4 Discussion and conclusions

In this study, we identify a mechanism that redistributes energy from the tropics to the extratropics via an accelerated BDC due to stratospheric heating. Using MPI-ESM simulations of idealized CO₂ and aerosol forcing, we explain the pronounced WP cooling as a result of stratospheric aerosol forcing, along with the strongly negative forcing it causes at the WP surface. This finding enhances our understanding of the formation of the WP-enhanced temperature change pattern in response to stratospheric aerosol forcing, which has previously been shown to cause strongly negative feedback (Günther et al., 2022; Salvi et al., 2023; Zhou et al., 2023).

The effective forcing from stratospheric aerosol is more negative in the WP than in the global mean already at the TOA. Furthermore, there is a substantial export of energy from the tropics to the extratropics via the stratosphere, effectively removing additional energy from the tropical surface. The stratospheric energy export emanates mainly from an acceleration of the BDC, which leads to increased adiabatic cooling in the tropical stratosphere and adiabatic heating in the extratropical stratosphere. Changes in the BDC ultimately arise from the differential heating between the tropical and the extratropical stratosphere, which affects wave activity and therefore the strength of the stratospheric pump (Holton et al., 1995; Graf et al., 2007; Schnadt Poberaj et al., 2011).

The time-constant forcing we use to model stratospheric aerosol forcing is reminiscent of strategies to cool the Earth with solar radiation management by deliberate injection of reflective aerosol into the stratosphere. Depending on the location and absorptivity of the used aerosol, the BDC will accelerate and lead to stronger cooling of the tropics than the extratropics. Tropical overcooling is a notorious problem in solar radiation management unless more sophisticated injection strategies are used (Laakso et al., 2017; Kravitz et al.,

2019). The importance of the BDC for the climate response corroborates the finding from previous studies that solar dimming is an imperfect substitute for simulating aerosol forcing (Ferraro et al., 2014; Simpson et al., 2019; Visionsi et al., 2021).

In order to highlight differences between aerosol and CO₂ forcing independently of the forcing pattern, we created a patterned CO₂ simulation, which approximately reproduces the TOA effective-forcing pattern of stratospheric aerosol. This was achieved by varying the CO₂ concentration in space and time. The aerosol and the patterned CO₂ simulation have more negative TOA radiative forcing in the WP and the tropics than in the global mean. Despite their similar TOA effective-forcing patterns, they exhibit substantial temperature pattern differences. We, therefore, argue that the increased energy export out of the tropics due to the acceleration of the BDC is essential for the emergence of the tropically enhanced temperature change pattern and the strong feedback to stratospheric aerosol forcing. This shows that the TOA-forcing perspective is not sufficient to explain the temperature patterns. The TOA perspective has previously been used as an explanation for the feedback to aerosol forcing (Salvi et al., 2022, 2023) and to solar forcing (Kaur et al., 2023; Modak et al., 2016) and for temperature change patterns in general (Liu et al., 2022). We show that the temperature pattern is more closely linked to the pattern of forcing at the surface than at the TOA. The TOA-forcing perspective is established in climate science, which is appropriate as long as the focus is on global means, but the patterns of TOA and surface forcing can be substantially different. Differences between them arise from changes in the atmospheric heat transport, which lead to a considerable redistribution of forcing between different regions of the Earth. This should be kept in mind when addressing the relationship between forcing patterns and temperature change patterns in future studies.

The comparison of radiatively forced simulations with simulations that were forced with an equivalent heat flux forcing at the surface reveals the existence of a link between the surface forcing pattern and the surface temperature response. Stronger surface forcing in the WP produces a stronger temperature change in the WP. Still, knowledge of the surface effective forcing in our simulations is not enough to reproduce the exact temperature response.

For the interpretation of our results, it should be kept in mind that the aerosol in our model has a highly idealized profile with no seasonal dependence and is not transported. The ozone profile is fixed, although ozone is affected by the presence of aerosol and has been shown to affect the BDC (Garfinkel et al., 2017; Pitari and Rizi, 1993; Schnadt Poberaj et al., 2011). Comparing aerosol-forced simulations in a single model with and without interactive ozone chemistry, Richter et al. (2017) find slightly higher upper-stratospheric upwelling in the simulation without atmospheric chemistry and almost no tropical temperature differences.

Furthermore, shifting the aerosol profile in altitude or latitude would likely modify the effect on the BDC so that our results may be dependent on the specific aerosol profile we choose. Aerosol that is injected at greater altitudes has been found to cause less negative feedback (Zhao et al., 2021; Lee et al., 2023). Lower injections allow more water vapor to enter the stratosphere because they more strongly affect cold-point temperatures. Lee et al. (2023) argue that this leads to a negative water vapor feedback. Since the increased stratospheric water vapor from cold-point heating appears on a timescale of months (Kroll et al., 2021) and independently of surface temperature, we suggest that this does not constitute a feedback but rather an adjustment. According to our results, the altitude dependence of the feedback could be related to the altitude dependence of the effect of stratospheric heating on the BDC. In addition to the dependence of feedback on altitude, we also expect a dependence on the meridional profile. Extratropical eruptions would not only cause a less WP-enhanced TOA-forcing pattern; they would also affect the BDC differently (Richter et al., 2017) and might therefore lack the WP enhancement of the surface forcing. Our results are, therefore, not necessarily applicable to aerosol forcing with pronounced hemispheric asymmetries.

In recent years, much progress has been made in understanding how patterns of SST affect radiative fluxes. In particular, SST Green's functions provide a detailed picture of the importance of tropical convective regions for radiative feedbacks. However, less is known about how these SST patterns come about. Simulations with q -flux Green's functions and slab ocean and pacemaker experiments indicate that heat fluxes over the Southern Ocean play an elevated role in SST pattern formation (Lin et al., 2021; Liu et al., 2018a, b, 2022; Hwang et al., 2017; Hu et al., 2022; Kang et al., 2023). Dynamic ocean and atmosphere processes make the temperature pattern time-dependent, even for constant forcings (Heede et al., 2020). Yet, the mechanistic picture of the connection between forcing patterns and SST patterns is still incomplete. While many pieces are missing in terms of completing this picture, we contribute to filling this gap by identifying relevant processes that cause differences between TOA and surface forcing, emphasizing the relevance of the latter, and by pointing out the atmospheric pathway from TOA forcing to surface forcing to surface temperature patterns, specifically for stratospheric aerosol forcing.

Appendix A: Finding a field of CO₂ concentrations that matches the effective TOA forcing of aerosol

A1 Approach

The goal is to find a field of CO₂ concentrations whose effective forcing is equal to the effective-forcing field from the stratospheric aerosol (Aero), which is known. The idea of the algorithm is to start with an initial guess; compute its effective forcing; and then iteratively increase the CO₂ con-

centration wherever the effective forcing is too negative and decrease it wherever the effective forcing is too positive, taking into account the logarithmic dependence of forcing on CO₂ concentration.

A2 Algorithm

Let x be the CO₂ concentration in units of the pre-industrial CO₂ concentration (284 ppm) as a function of longitude, latitude, and time. The goal is to find a target field x_t , whose effective TOA forcing F matches a given target F_t . The indices i and t will be used in the following to indicate initial and target fields.

Instantaneous CO₂ radiative forcing approximately follows the relationship

$$F \approx c \cdot \log_2(x). \quad (\text{A1})$$

Equation (A1) holds approximately in terms of the global mean, with $c \approx 3.7 \text{ W m}^{-2}$ (Myhre et al., 1998). However, the instantaneous radiative forcing at each location is determined by the local difference between the temperatures at the surface and the tropopause (Jeevanjee et al., 2021), resulting in a non-uniform TOA instantaneous-forcing pattern, even for a uniform change in CO₂ concentration. Atmospheric adjustments and noise cause further departures of the effective forcing from the instantaneous forcing, both in terms of its pattern and global mean.

From Eq. (A1), it follows that

$$F_t/F_i \approx \log_2(x_t)/\log_2(x_i), \quad (\text{A2})$$

$$x_t \approx 2^{F_t/F_i \cdot \log_2(x_i)}, \quad (\text{A3})$$

$$x_t = x_i^{F_t/F_i} + \epsilon. \quad (\text{A4})$$

See also Xia and Huang (2017). In the last step, the approximation symbol is replaced by inclusion of an error term ϵ . The effective-forcing field F of any forcing can be computed as the difference in TOA fluxes between a perturbed and an unperturbed simulation with fixed SST and sea ice. Therefore, for any x_i , F_i can be determined. Using Eq. (A4), one can compute a field x_t that will have the desired forcing field F_t up to an error term ϵ . Using x_t as the new x_i , ϵ can be minimized by repeatedly applying Eq. (A4) to each horizontal grid point. The target F_t remains the same in all iterations.

It is not clear a priori that this algorithm converges. In fact, a few modifications must be made due to errors from adjustments and noise. We apply these modifications in every step.

1. In Eq. (A4), $F_t/F_i \rightarrow \pm\infty$ for $F_i \rightarrow 0$. To address this problem we set F_i in the calculation to $\pm 0.5 \text{ W m}^{-2}$ wherever its absolute value is smaller than 0.5 W m^{-2} .
2. In our specific case, F_t is generally negative, but it is positive in some places, especially near the poles. In the case where $F_i < 0 < F_t$, problems arise when $x_i > 1$. From Eq. (A1), this is not generally expected ($x_i > 1$ is

associated with $F_i > 0$) but can happen due to adjustments or noise. This violation of the assumptions leads to local divergence of the algorithm. One way to fix this is to set $x_t = x_i + c$ wherever $F_i < 0 < F_t \wedge x_i > 1$ instead of applying Eq. (A4). We arbitrarily choose $c = 0.5$. The idea is to force the algorithm to increase the CO₂ concentration when it is too low in cases where it would normally decrease it. Similarly, we set $x_t = x_i - c$ wherever $F_i > 0 > F_t \wedge x_i < 1$ to account for the opposite case.

3. After applying Eq. (A4), we apply a moving-average filter to $\log_2(x)$ with a window length of 19° latitude and 36° longitude in order to smooth the spatial variations.
4. After the moving-average filter, we restrict CO₂ concentrations to $1/4 < x_t < 4$ in the interest of avoiding too-extreme variations.

With the modifications in place, the algorithm converged according to our subjective judgment after three iterations. The resulting field of CO₂ concentrations is shown in Fig. 2b of the main text, and the effective TOA-forcing field is shown in Fig. 3a of the main text. Both clearly share large-scale features, e.g., the most negative forcing and the most strongly reduced CO₂ concentration over the WP, but they differ on smaller scales due to adjustments and noise. Monthly mean fields of effective TOA forcing and CO₂ concentrations of pCO₂ in comparison to Aero are shown in Figs. A1 and A2.

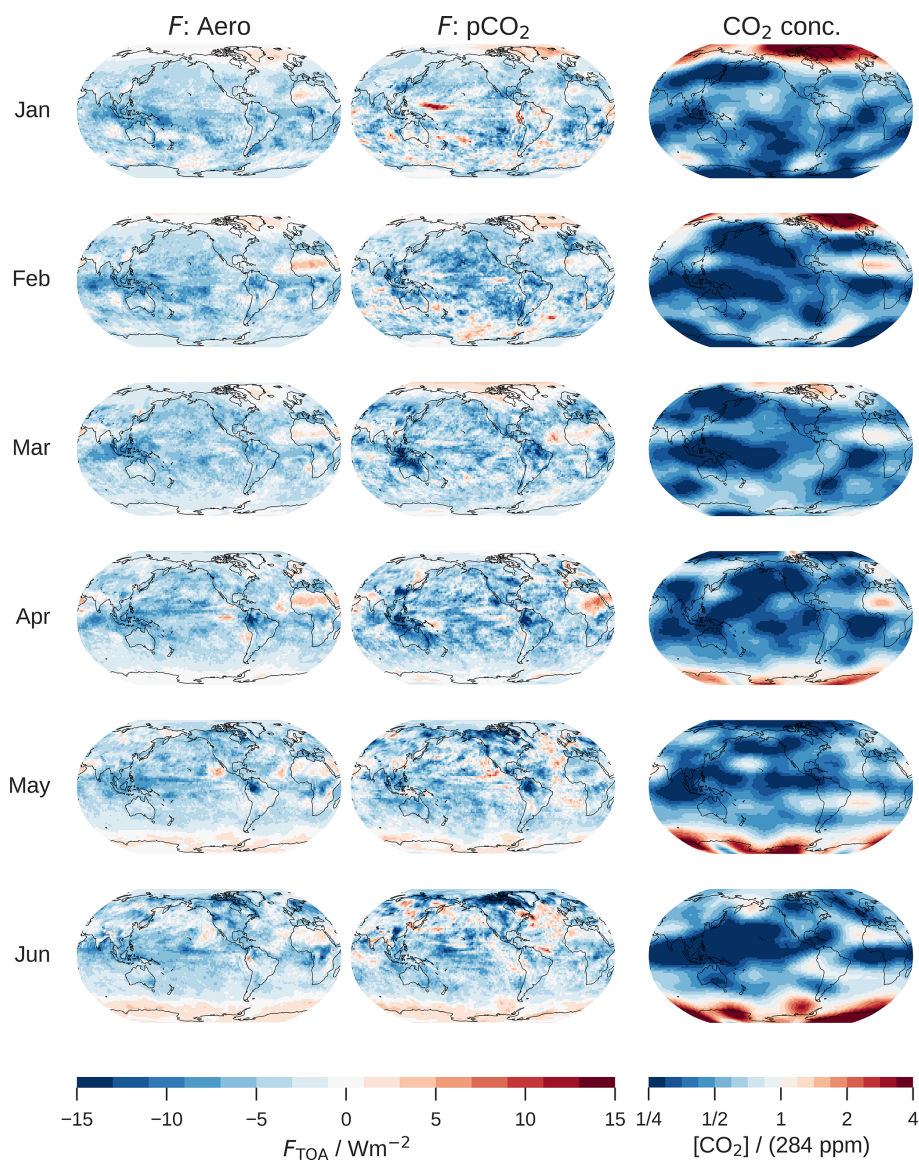


Figure A1. Monthly comparison of the effective TOA forcings of Aero and pCO₂: January–June. The right column shows the field of CO₂ concentrations that results in the effective forcing of the middle column. Note the seasonal dependence of the forcing, with positive forcing over the pole of the winter hemisphere. The seasonal dependence arises despite the time-invariant aerosol profile from the seasonally varying insolation.

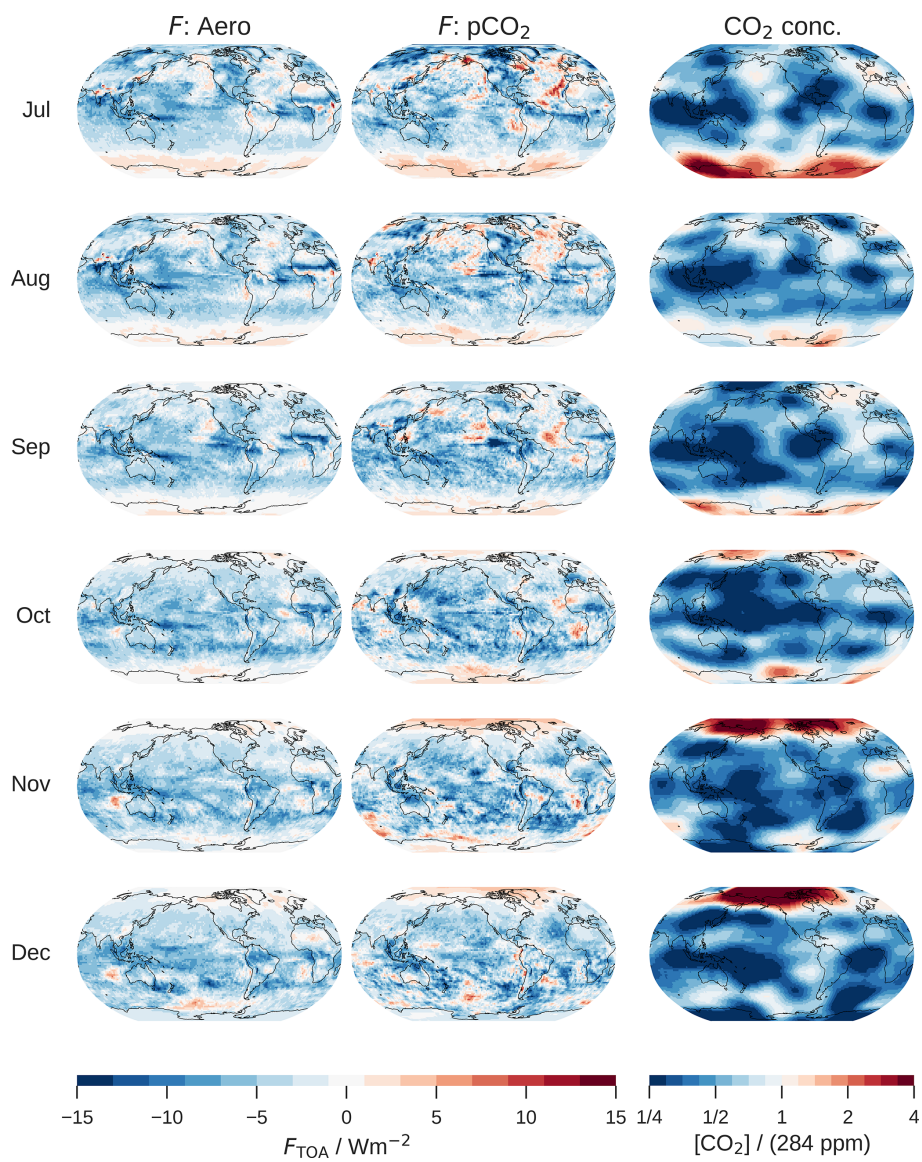


Figure A2. Same as Fig. A1 but for July–December.

Appendix B: Tropical–zonal circulation from ocean to land

Although not the main focus of this study, we provide a short explanation as to why there is a tropical–zonal energy transport from the WP to tropical non-WP regions in all fixed-SST simulations (see Sect. 3.3 of the main text).

Figure B1 shows histograms of variables that indicate an anomalous ocean–land circulation in the fixed-SST simulations. Over land, the atmosphere loses energy by radiative and turbulent fluxes almost everywhere because the land can cool down in the fixed-SST simulation, while the ocean can not. This energy loss is compensated for by adiabatic heating due to the more pronounced downward motion over land.

The energy that is transported to the atmosphere over land is supplied from the atmosphere over the ocean, which gains more energy from turbulent and radiative fluxes. The air rises more strongly over the ocean, associated with more precipitation and, hence, convective heating. The circulation must necessarily be closed by the movement of air from ocean to land aloft and from land to ocean near the surface.

The top and middle rows show that the WP ocean regions provide proportionally more energy than the tropical non-WP ocean regions, indicated by more positive forcing in the atmosphere and a stronger increase in precipitation. Since the WP is a major region of deep convection, it effectively couples the surface to the free troposphere, which enables energy transport from the surface to the free troposphere and subsequently to the land regions. The prevailing inversion over, e.g., the eastern Pacific impedes this energy transport. Therefore, the majority of the energy transport happens from WP ocean regions to land regions.

This picture is qualitatively similar for the Aero, $0.5\times\text{CO}_2$, and pCO_2 simulations because it does not directly depend on the presence of the forcing agent. Instead, it emerges as a consequence of the air–sea contrast that arises from fixing SST but not land temperatures. A real-world analog might be the fast response to forcing, where land temperatures react more quickly than SST, such as after volcanic eruptions.

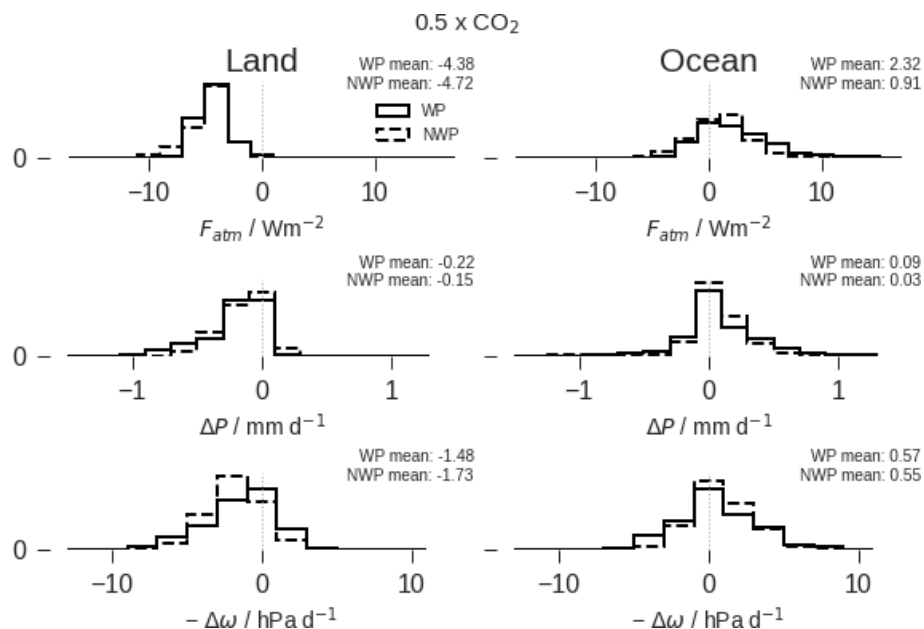


Figure B1. Distribution of changes over the tropics, separated into land–ocean and WP–tropical non-WP regions, indicating an ocean–land circulation. Values are taken from the 0.5× CO₂ simulation (Aero and pCO₂ are qualitatively similar). All histograms show changes in the fixed-SST simulation compared to piClim-control. Top: effective forcing on the atmosphere (TOA–surface forcing). Middle: precipitation. Bottom: negative pressure velocity at 500 hPa (positive values indicate rising motion). NWP refers to tropical non-WP regions.

Appendix C: Components of the TOA forcing of Aero

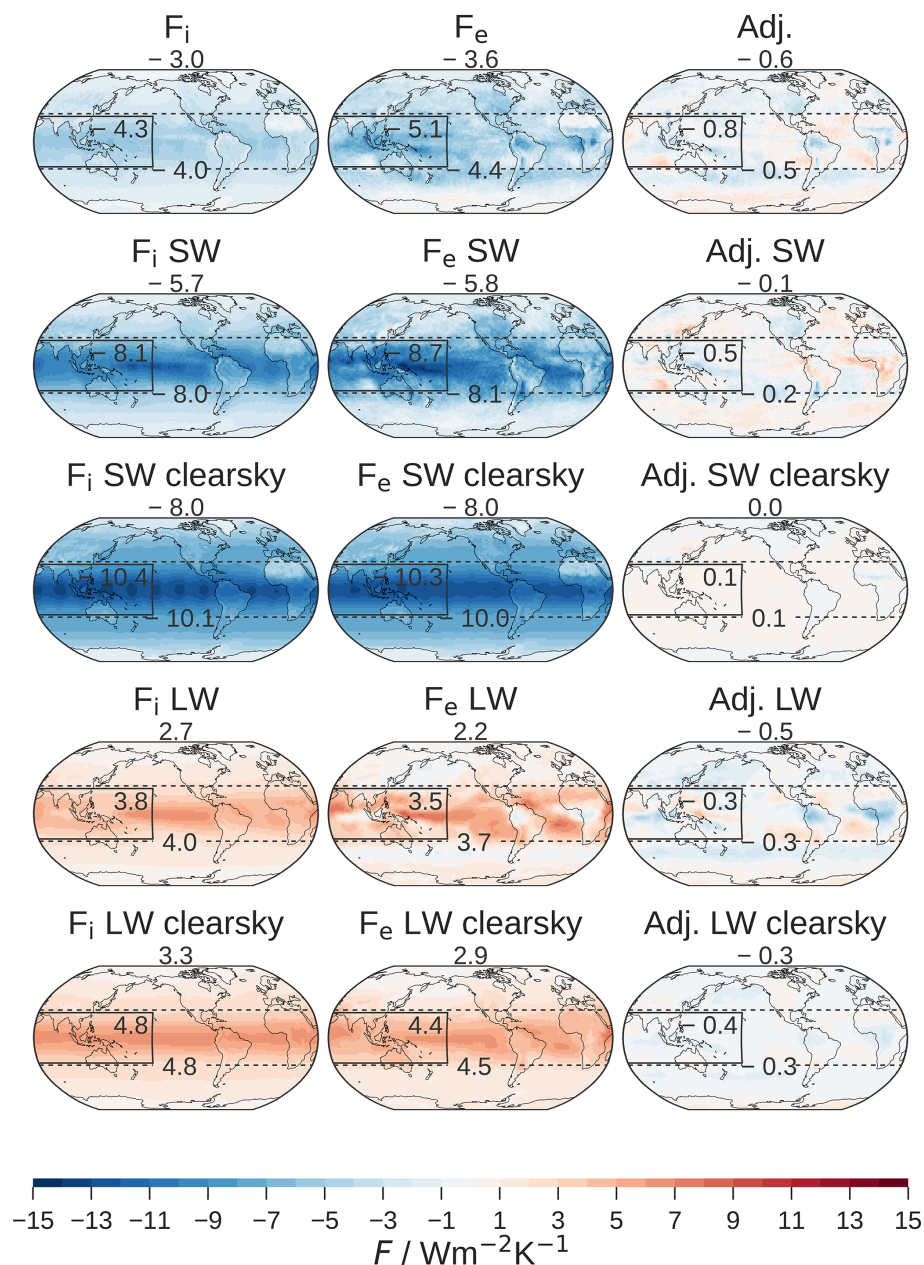


Figure C1. For Aero, we show instantaneous forcing (first column) and effective forcing (second column), as well as the difference between the two (adjustments, third column). We further split this into SW and LW contributions and separate out the clear sky.

Appendix D: CMIP6 models

Table D1. CMIP6 models with historical simulations included in the CMIP analysis.

	Ensemble members
ACCESS-CM2	3
BCC-CSM2-MR	3
BCC-ESM1	3
CESM2-FV2	3
CESM2-WACCM-FV2	3
CESM2-WACCM	3
CIESM	3
CMCC-CM2-SR5	1
CNRM-CM6-1-HR	1
CanESM5	65
FGOALS-f3-L	3
FGOALS-g3	6
GFDL-CM4	1
GFDL-ESM4	3
GISS-E2-1-G	47
GISS-E2-1-H	25
INM-CM4-8	1
INM-CM5-0	10
MIROC6	50
NESM3	5
NorESM2-MM	3
SAM0-UNICON	1
TaiESM1	1

Code and data availability. The code and data used for this study are available from <https://hdl.handle.net/21.14106/1817cc7171b9b4e20af34a716a0de8b3fa275a6e> (Günther, 2024).

Author contributions. MG and HS conceived this study, building on ideas formulated by HS, CT, and MT. MG performed the simulations and the analysis and wrote the initial paper draft. All authors discussed the results and revised the paper together.

Competing interests. At least one of the (co-)authors is a member of the editorial board of *Atmospheric Chemistry and Physics*. The peer-review process was guided by an independent editor, and the authors also have no other competing interests to declare.

Disclaimer. Publisher's note: Copernicus Publications remains neutral with regard to jurisdictional claims made in the text, published maps, institutional affiliations, or any other geographical representation in this paper. While Copernicus Publications makes every effort to include appropriate place names, the final responsibility lies with the authors.

Acknowledgements. This work used resources of the Deutsches Klimarechenzentrum (DKRZ), granted by its Scientific Steering Committee (WLA) under project ID no. mh0066. We acknowledge the World Climate Research Programme, which, through its Working Group on Coupled Modeling, coordinated and promoted CMIP6. We thank the climate modeling groups for producing and making available their model output, the Earth System Grid Federation (ESGF) for archiving the data and providing access, and the multiple funding agencies who support CMIP6 and ESGF. We thank Dirk Olonschek for the detailed and helpful comments on an earlier version of the paper. Additionally, we would like to thank Chen Zhou, Daniele Visioni, and an anonymous reviewer for their constructive feedback that improved the paper.

Financial support. This research has been supported by German National funding agency (DFG) research unit FOR 2820: Revisiting The Volcanic Impact on Atmosphere and Climate-Preparations for the Next Big Volcanic Eruption (VolImpact, grant no. 545 398006378).

The article processing charges for this open-access publication were covered by the Max Planck Society.

Review statement. This paper was edited by Paulo Ceppi and reviewed by Daniele Visioni, Chen Zhou, and one anonymous referee.

References

- Abalos, M., Legras, B., Ploeger, F., and Randel, W. J.: Evaluating the advective Brewer-Dobson circulation in three reanalyses for the period 1979–2012, *J. Geophys. Res.-Atmos.*, 120, 7534–7554, <https://doi.org/10.1002/2015JD023182>, 2015.
- Aquila, V., Oman, L. D., Stolarski, R., Douglass, A. R., and Newman, P. A.: The Response of Ozone and Nitrogen Dioxide to the Eruption of Mt. Pinatubo at Southern and Northern Midlatitudes, *J. Atmos. Sci.*, 70, 894–900, <https://doi.org/10.1175/JAS-D-12-0143.1>, 2013.
- Azoulay, A., Schmidt, H., and Timmreck, C.: The Arctic Polar Vortex Response to Volcanic Forcing of Different Strengths, *J. Geophys. Res.-Atmos.*, 126, e2020JD034450, <https://doi.org/10.1029/2020JD034450>, 2021.
- Birner, T. and Charlesworth, E. J.: On the relative importance of radiative and dynamical heating for tropical tropopause temperatures, *J. Geophys. Res.-Atmos.*, 122, 6782–6797, <https://doi.org/10.1002/2016JD026445>, 2017.
- Bittner, M., Schmidt, H., Timmreck, C., and Sienz, F.: Using a large ensemble of simulations to assess the Northern Hemisphere stratospheric dynamical response to tropical volcanic eruptions and its uncertainty, *Geophys. Res. Lett.*, 43, 9324–9332, <https://doi.org/10.1002/2016GL070587>, 2016.
- Bony, S., Colman, R., Kattsov, V. M., Allan, R. P., Bretherton, C. S., Dufresne, J.-L., Hall, A., Hallegatte, S., Holland, M. M., Ingram, W., Randall, D. A., Soden, B. J., Tselioudis, G., and Webb, M. J.: How Well Do We Understand and Evaluate Climate Change Feedback Processes?, *J. Climate*, 19, 3445–3482, <https://doi.org/10.1175/JCLI3819.1>, 2006.

- Butchart, N.: The Brewer-Dobson circulation, *Rev. Geophys.*, 52, 157–184, <https://doi.org/10.1002/2013RG000448>, 2014.
- Ceppi, P. and Gregory, J. M.: A Refined Model for the Earth's Global Energy Balance, *Clim. Dynam.*, 53, 4781–4797, <https://doi.org/10.1007/s00382-019-04825-x>, 2019.
- Diallo, M., Legras, B., and Chédin, A.: Age of stratospheric air in the ERA-Interim, *Atmos. Chem. Phys.*, 12, 12133–12154, <https://doi.org/10.5194/acp-12-12133-2012>, 2012.
- Diallo, M., Ploeger, F., Konopka, P., Birner, T., Müller, R., Riese, M., Garny, H., Legras, B., Ray, E., Berthet, G., and Jegou, F.: Significant Contributions of Volcanic Aerosols to Decadal Changes in the Stratospheric Circulation, *Geophys. Res. Lett.*, 44, 10780–10791, <https://doi.org/10.1002/2017GL074662>, 2017.
- Dong, Y., Proistosescu, C., Armour, K. C., and Battisti, D. S.: Attributing Historical and Future Evolution of Radiative Feedbacks to Regional Warming Patterns using a Green's Function Approach: The Preeminence of the Western Pacific, *J. Climate*, 32, 5471–5491, <https://doi.org/10.1175/JCLI-D-18-0843.1>, 2019.
- Eyring, V., Bony, S., Meehl, G. A., Senior, C. A., Stevens, B., Stouffer, R. J., and Taylor, K. E.: Overview of the Coupled Model Intercomparison Project Phase 6 (CMIP6) experimental design and organization, *Geosci. Model Dev.*, 9, 1937–1958, <https://doi.org/10.5194/gmd-9-1937-2016>, 2016.
- Fajber, R. and Kushner, P. J.: Using “Heat Tagging” to Understand the Remote Influence of Atmospheric Diabatic Heating through Long-Range Transport, *J. Atmos. Sci.*, 78, 2161–2176, <https://doi.org/10.1175/JAS-D-20-0290.1>, 2021.
- Fajber, R., Donohoe, A., Ragen, S., Armour, K. C., and Kushner, P. J.: Atmospheric heat transport is governed by meridional gradients in surface evaporation in modern-day earth-like climates, *P. Natl. Acad. Sci. USA*, 120, e2217202120, <https://doi.org/10.1073/pnas.2217202120>, 2023.
- Ferraro, A. J., Highwood, E. J., and Charlton-Perez, A. J.: Weakened tropical circulation and reduced precipitation in response to geoengineering, *Environ. Res. Lett.*, 9, 014001, <https://doi.org/10.1088/1748-9326/9/1/014001>, 2014.
- Forster, P. M., Richardson, T., Maycock, A. C., Smith, C. J., Samset, B. H., Myhre, G., Andrews, T., Pincus, R., and Schulz, M.: Recommendations for Diagnosing Effective Radiative Forcing from Climate Models for CMIP6, *J. Geophys. Res.-Atmos.*, 121, 12460–12475, <https://doi.org/10.1002/2016JD025320>, 2016.
- Garcia, R. R. and Randel, W. J.: Acceleration of the Brewer-Dobson Circulation due to Increases in Greenhouse Gases, *J. Atmos. Sci.*, 65, 2731–2739, <https://doi.org/10.1175/2008JAS2712.1>, 2008.
- Garcia, R. R., Randel, W. J., and Kinnison, D. E.: On the Determination of Age of Air Trends from Atmospheric Trace Species, *J. Atmos. Sci.*, 68, 139–154, <https://doi.org/10.1175/2010JAS3527.1>, 2011.
- Garfinkel, C. I., Aquila, V., Waugh, D. W., and Oman, L. D.: Time-varying changes in the simulated structure of the Brewer-Dobson Circulation, *Atmos. Chem. Phys.*, 17, 1313–1327, <https://doi.org/10.5194/acp-17-1313-2017>, 2017.
- Graf, H.-F., Li, Q., and Giorgetta, M. A.: Volcanic effects on climate: revisiting the mechanisms, *Atmos. Chem. Phys.*, 7, 4503–4511, <https://doi.org/10.5194/acp-7-4503-2007>, 2007.
- Gregory, J. M. and Andrews, T.: Variation in Climate Sensitivity and Feedback Parameters during the Historical Period, *Geophys. Res. Lett.*, 43, 3911–3920, <https://doi.org/10.1002/2016GL068406>, 2016.
- Gregory, J. M., Andrews, T., Good, P., Mauritsen, T., and Forster, P. M.: Small Global-Mean Cooling Due to Volcanic Radiative Forcing, *Clim. Dynam.*, 47, 3979–3991, <https://doi.org/10.1007/s00382-016-3055-1>, 2016.
- Gregory, J. M., Andrews, T., Ceppi, P., Mauritsen, T., and Webb, M. J.: How Accurately Can the Climate Sensitivity to CO₂ Be Estimated from Historical Climate Change?, *Clim. Dynam.*, 54, 129–157, <https://doi.org/10.1007/s00382-019-04991-y>, 2020.
- Günther, M.: Code and model output for “Why does stratospheric aerosol forcing strongly cool the warm pool?”, DOKU at DKRZ [code, data set], <https://hdl.handle.net/21.14106/1817cc7171b9b4e20af34a716a0de8b3fa275a6e>, 2024.
- Günther, M., Schmidt, H., Timmreck, C., and Toohey, M.: Climate Feedback to Stratospheric Aerosol Forcing: The Key Role of the Pattern Effect, *J. Climate*, 35, 4303–4317, <https://doi.org/10.1175/JCLI-D-22-0306.1>, 2022.
- Hansen, J., Sato, M., and Ruedy, R.: Radiative Forcing and Climate Response, *J. Geophys. Res.-Atmos.*, 102, 6831–6864, <https://doi.org/10.1029/96JD03436>, 1997.
- Hansen, J., Sato, M., Ruedy, R., Nazarenko, L., Schmidt, G. A., Russell, G., Aleinov, I., Bauer, M., Bauer, S., Bell, N., Cairns, B., Canuto, V., Chandler, M., Cheng, Y., Del Genio, A., Faluvegi, G., Fleming, E., Friend, A., Hall, T., Jackman, C., Kelley, M., Klang, N., Koch, D., Lean, J., Lerner, J., Lo, K., Menon, S., Miller, R., Minnis, P., Novakov, T., Oinas, V., Perlwitz, J., Rind, D., Romanou, A., Shindell, D., Stone, P., Sun, S., Tausnev, N., Thresher, D., Wielicki, B., Wong, T., Yao, M., and Zhang, S.: Efficacy of Climate Forcings, *J. Geophys. Res.*, 110, D18104, <https://doi.org/10.1029/2005JD005776>, 2005.
- Haugstad, A. D., Armour, K. C., Battisti, D. S., and Rose, B. E. J.: Relative Roles of Surface Temperature and Climate Forcing Patterns in the Inconstancy of Radiative Feedbacks, *Geophys. Res. Lett.*, 44, 7455–7463, <https://doi.org/10.1002/2017GL074372>, 2017.
- Heede, U. K., Fedorov, A. V., and Burls, N. J.: Time Scales and Mechanisms for the Tropical Pacific Response to Global Warming: A Tug of War between the Ocean Thermostat and Weaker Walker, *J. Climate*, 33, 6101–6118, <https://doi.org/10.1175/JCLI-D-19-0690.1>, 2020.
- Holton, J. R., Haynes, P. H., McIntyre, M. E., Douglass, A. R., Rood, R. B., and Pfister, L.: Stratosphere-troposphere exchange, *Rev. Geophys.*, 33, 403–439, <https://doi.org/10.1029/95RG02097>, 1995.
- Hu, S., Xie, S.-P., and Kang, S. M.: Global Warming Pattern Formation: The Role of Ocean Heat Uptake, *J. Climate*, 35, 1885–1899, <https://doi.org/10.1175/JCLI-D-21-0317.1>, 2022.
- Hwang, Y.-T., Xie, S.-P., Deser, C., and Kang, S. M.: Connecting tropical climate change with Southern Ocean heat uptake, *Geophys. Res. Lett.*, 44, 9449–9457, <https://doi.org/10.1002/2017GL074972>, 2017.
- Ilyina, T., Six, K. D., Segsneider, J., Maier-Reimer, E., Li, H., and Núñez-Riboni, I.: Global ocean biogeochemistry model HAMOCC: Model architecture and performance as component of the MPI-Earth system model in different CMIP5 experimental realizations, *J. Adv. Model. Earth Sy.*, 5, 287–315, <https://doi.org/10.1029/2012MS000178>, 2013.
- Jeevanjee, N., Seeley, J. T., Paynter, D., and Fueglistaler, S.: An Analytical Model for Spatially Varying Clear-Sky CO₂ Forcing,

- J. Climate, 34, 9463–9480, <https://doi.org/10.1175/JCLI-D-19-0756.1>, 2021.
- Joshi, M. M. and Shine, K. P.: A GCM Study of Volcanic Eruptions as a Cause of Increased Stratospheric Water Vapor, *J. Climate*, 16, 3525–3534, [https://doi.org/10.1175/1520-0442\(2003\)016<3525:AGSOVE>2.0.CO;2](https://doi.org/10.1175/1520-0442(2003)016<3525:AGSOVE>2.0.CO;2), 2003.
- Jungclaus, J. H., Fischer, N., Haak, H., Lohmann, K., Marotzke, J., Matei, D., Mikolajewicz, U., Notz, D., and von Storch, J. S.: Characteristics of the ocean simulations in the Max Planck Institute Ocean Model (MPIOM) the ocean component of the MPI-Earth system model, *J. Adv. Model. Earth Sy.*, 5, 422–446, <https://doi.org/10.1002/jame.20023>, 2013.
- Kang, S. M., Ceppi, P., Yu, Y., and Kang, I.-S.: Recent global climate feedback controlled by Southern Ocean cooling, *Nat. Geosci.*, 16, 775–780, <https://doi.org/10.1038/s41561-023-01256-6>, 2023.
- Kaur, H., Bala, G., and Seshadri, A. K.: Why Is Climate Sensitivity for Solar Forcing Smaller than for an Equivalent CO₂ Forcing?, *J. Climate*, 36, 775–789, <https://doi.org/10.1175/JCLI-D-21-0980.1>, 2023.
- Kravitz, B., MacMartin, D. G., Tilmes, S., Richter, J. H., Mills, M. J., Cheng, W., Dagon, K., Glanville, A. S., Lamarque, J.-F., Simpson, I. R., Tribbia, J., and Vitt, F.: Comparing Surface and Stratospheric Impacts of Geoengineering With Different SO₂ Injection Strategies, *J. Geophys. Res.-Atmos.*, 124, 7900–7918, <https://doi.org/10.1029/2019JD030329>, 2019.
- Kroll, C. A., Dacie, S., Azoulay, A., Schmidt, H., and Timmreck, C.: The impact of volcanic eruptions of different magnitude on stratospheric water vapor in the tropics, *Atmos. Chem. Phys.*, 21, 6565–6591, <https://doi.org/10.5194/acp-21-6565-2021>, 2021.
- Laakso, A., Korhonen, H., Romakkaniemi, S., and Kokkola, H.: Radiative and climate effects of stratospheric sulfur geoengineering using seasonally varying injection areas, *Atmos. Chem. Phys.*, 17, 6957–6974, <https://doi.org/10.5194/acp-17-6957-2017>, 2017.
- Lee, W. R., Visioni, D., Bednarz, E. M., MacMartin, D. G., Kravitz, B., and Tilmes, S.: Quantifying the Efficiency of Stratospheric Aerosol Geoengineering at Different Altitudes, *Geophys. Res. Lett.*, 50, e2023GL104417, <https://doi.org/10.1029/2023GL104417>, 2023.
- Lin, Y.-J., Hwang, Y.-T., Lu, J., Liu, F., and Rose, B. E. J.: The Dominant Contribution of Southern Ocean Heat Uptake to Time-Evolving Radiative Feedback in CESM, *Geophys. Res. Lett.*, 48, e2021GL093302, <https://doi.org/10.1029/2021GL093302>, 2021.
- Liu, F., Lu, J., Garuba, O., Leung, L. R., Luo, Y., and Wan, X.: Sensitivity of Surface Temperature to Oceanic Forcing via q-Flux Green's Function Experiments. Part I: Linear Response Function, *J. Climate*, 31, 3625–3641, <https://doi.org/10.1175/JCLI-D-17-0462.1>, 2018a.
- Liu, F., Lu, J., Garuba, O. A., Huang, Y., Leung, L. R., Harrop, B. E., and Luo, Y.: Sensitivity of Surface Temperature to Oceanic Forcing via q-Flux Green's Function Experiments. Part II: Feedback Decomposition and Polar Amplification, *J. Climate*, 31, 6745–6761, <https://doi.org/10.1175/JCLI-D-18-0042.1>, 2018b.
- Liu, F., Lu, J., and Leung, L. R.: Neutral Mode Dominates the Forced Global and Regional Surface Temperature Response in the Past and Future, *Geophys. Res. Lett.*, 49, e2022GL098788, <https://doi.org/10.1029/2022GL098788>, 2022.
- Marshall, L. R., Smith, C. J., Forster, P. M., Aubry, T. J., Andrews, T., and Schmidt, A.: Large Variations in Volcanic Aerosol Forcing Efficiency Due to Eruption Source Parameters and Rapid Adjustments, *Geophys. Res. Lett.*, 47, e2020GL090241, <https://doi.org/10.1029/2020GL090241>, 2020.
- Mauritsen, T., Bader, J., Becker, T., Behrens, J., Bittner, M., Brokopf, R., Brovkin, V., Claussen, M., Crueger, T., Esch, M., Fast, I., Fiedler, S., Fläschner, D., Gayler, V., Giorgetta, M., Goll, D. S., Haak, H., Hagemann, S., Hedemann, C., Hohenegger, C., Ilyina, T., Jahns, T., Jimenez-de-la Cuesta, D., Jungclaus, J., Kleinen, T., Kloster, S., Kracher, D., Kinne, S., Kleberg, D., Lasslop, G., Kornblueh, L., Marotzke, J., Matei, D., Meraner, K., Mikolajewicz, U., Modali, K., Möbis, B., Müller, W. A., Nabel, J. E. M. S., Nam, C. C. W., Notz, D., Nyawira, S.-S., Paulsen, H., Peters, K., Pincus, R., Pohlmann, H., Pongratz, J., Popp, M., Raddatz, T. J., Rast, S., Redler, R., Reick, C. H., Rohrschneider, T., Schemann, V., Schmidt, H., Schnur, R., Schulzweida, U., Six, K. D., Stein, L., Stemmler, I., Stevens, B., von Storch, J.-S., Tian, F., Voigt, A., Vrese, P., Wieners, K.-H., Wilkenskjaeld, S., Winkler, A., and Roeckner, E.: Developments in the MPI-M Earth System Model version 1.2 (MPI-ESM1.2) and Its Response to Increasing CO₂, *J. Adv. Model. Earth Sy.*, 11, 998–1038, <https://doi.org/10.1029/2018MS001400>, 2019.
- McMonigal, K., Larson, S., Hu, S., and Kramer, R.: Historical Changes in Wind-Driven Ocean Circulation Can Accelerate Global Warming, *Geophys. Res. Lett.*, 50, e2023GL102846, <https://doi.org/10.1029/2023GL102846>, 2023.
- Modak, A., Bala, G., Cao, L., and Caldeira, K.: Why Must a Solar Forcing Be Larger than a CO₂ Forcing to Cause the Same Global Mean Surface Temperature Change?, *Environ. Res. Lett.*, 11, 044013, <https://doi.org/10.1088/1748-9326/11/4/044013>, 2016.
- Muthers, S., Kuchar, A., Stenke, A., Schmitt, J., Anet, J. G., Raible, C. C., and Stocker, T. F.: Stratospheric age of air variations between 1600 and 2100, *Geophys. Res. Lett.*, 43, 5409–5418, <https://doi.org/10.1002/2016GL068734>, 2016.
- Myhre, G., Highwood, E. J., Shine, K. P., and Stordal, F.: New Estimates of Radiative Forcing Due to Well Mixed Greenhouse Gases, *Geophys. Res. Lett.*, 25, 2715–2718, <https://doi.org/10.1029/98GL01908>, 1998.
- Pitari, G. and Mancini, E.: Short-term climatic impact of the 1991 volcanic eruption of Mt. Pinatubo and effects on atmospheric tracers, *Nat. Hazards Earth Syst. Sci.*, 2, 91–108, <https://doi.org/10.5194/nhess-2-91-2002>, 2002.
- Pitari, G. and Rizi, V.: An Estimate of the Chemical and Radiative Perturbation of Stratospheric Ozone Following the Eruption of Mt. Pinatubo, *J. Atmos. Sci.*, 50, 3260–3276, [https://doi.org/10.1175/1520-0469\(1993\)050<3260:AEOTCA>2.0.CO;2](https://doi.org/10.1175/1520-0469(1993)050<3260:AEOTCA>2.0.CO;2), 1993.
- Reick, C. H., Gayler, V., Goll, D., Hagemann, S., Heidkamp, M., Nabel, J. E. M. S., Raddatz, T., Roeckner, E., Schnur, R., and Wilkenskjaeld, S.: JSBACH 3 – The land component of the MPI Earth System Model: documentation of version 3.2, *MPI für Meteorologie*, <https://doi.org/10.17617/2.3279802>, 2021.
- Richter, J. H., Tilmes, S., Mills, M. J., Tribbia, J. J., Kravitz, B., MacMartin, D. G., Vitt, F., and Lamarque, J.-F.: Stratospheric Dynamical Response and Ozone Feedbacks in the Presence of SO₂ Injections, *J. Geophys. Res.-Atmos.*, 122, 12557–12573, <https://doi.org/10.1002/2017JD026912>, 2017.

- Rugenstein, M. A. A. and Armour, K. C.: Three Flavors of Radiative Feedbacks and Their Implications for Estimating Equilibrium Climate Sensitivity, *Geophys. Res. Lett.*, 48, e2021GL092983, <https://doi.org/10.1029/2021GL092983>, 2021.
- Salvi, P., Ceppi, P., and Gregory, J. M.: Interpreting Differences in Radiative Feedbacks From Aerosols Versus Greenhouse Gases, *Geophys. Res. Lett.*, 49, e2022GL097766, <https://doi.org/10.1029/2022GL097766>, 2022.
- Salvi, P., Gregory, J. M., and Ceppi, P.: Time-Evolving Radiative Feedbacks in the Historical Period, *J. Geophys. Res.-Atmos.*, 128, e2023JD038984, <https://doi.org/10.1029/2023JD038984>, 2023.
- Schnadt Poberaj, C., Staehelin, J., and Brunner, D.: Missing Stratospheric Ozone Decrease at Southern Hemisphere Middle Latitudes after Mt. Pinatubo: A Dynamical Perspective, *J. Atmos. Sci.*, 68, 1922–1945, <https://doi.org/10.1175/JAS-D-10-05004.1>, 2011.
- Seviour, W. J. M., Butchart, N., and Hardiman, S. C.: The Brewer-Dobson circulation inferred from ERA-Interim, *Q. J. Roy. Meteor. Soc.* 138, 878–888, <https://doi.org/10.1002/qj.966>, 2012.
- Sherwood, S. C., Bony, S., Boucher, O., Bretherton, C., Forster, P. M., Gregory, J. M., and Stevens, B.: Adjustments in the Forcing-Feedback Framework for Understanding Climate Change, *B. Am. Meteor. Soc.*, 96, 217–228, <https://doi.org/10.1175/BAMS-D-13-00167.1>, 2015.
- Simpson, I. R., Tilmes, S., Richter, J. H., Kravitz, B., MacMartin, D. G., Mills, M. J., Fasullo, J. T., and Pendergrass, A. G.: The Regional Hydroclimate Response to Stratospheric Sulfate Geoengineering and the Role of Stratospheric Heating, *J. Geophys. Res.-Atmos.*, 124, 12587–12616, <https://doi.org/10.1029/2019JD031093>, 2019.
- SPARC: SPARC Reanalysis Intercomparison Project (SRIP) Final Report, SPARC Report 10, WCRP-6/2021, <https://doi.org/10.17874/800dec57d13>, 2022.
- Stevens, B., Giorgetta, M., Esch, M., Mauritsen, T., Crueger, T., Rast, S., Salzmann, M., Schmidt, H., Bader, J., Block, K., Brokopf, R., Fast, I., Kinne, S., Kornbluh, L., Lohmann, U., Pincus, R., Reichler, T., and Roeckner, E.: Atmospheric component of the MPI-M Earth System Model: ECHAM6, *J. Adv. Model. Earth Sy.*, 5, 146–172, <https://doi.org/10.1002/jame.20015>, 2013.
- Toohey, M., Krüger, K., Bittner, M., Timmreck, C., and Schmidt, H.: The impact of volcanic aerosol on the Northern Hemisphere stratospheric polar vortex: mechanisms and sensitivity to forcing structure, *Atmos. Chem. Phys.*, 14, 13063–13079, <https://doi.org/10.5194/acp-14-13063-2014>, 2014.
- Toohey, M., Stevens, B., Schmidt, H., and Timmreck, C.: Easy Volcanic Aerosol (EVA v1.0): an idealized forcing generator for climate simulations, *Geosci. Model Dev.*, 9, 4049–4070, <https://doi.org/10.5194/gmd-9-4049-2016>, 2016.
- Visioni, D., MacMartin, D. G., and Kravitz, B.: Is Turning Down the Sun a Good Proxy for Stratospheric Sulfate Geoengineering?, *J. Geophys. Res.-Atmos.*, 126, e2020JD033952, <https://doi.org/10.1029/2020JD033952>, 2021.
- Wunderlin, E., Chiodo, G., Sukhodolov, T., Vattioni, S., Visioni, D., and Tilmes, S.: Side Effects of Sulfur-Based Geoengineering Due To Absorptivity of Sulfate Aerosols, *Geophys. Res. Lett.*, 51, e2023GL107285, <https://doi.org/10.1029/2023GL107285>, 2024.
- Xia, Y. and Huang, Y.: Differential Radiative Heating Drives Tropical Atmospheric Circulation Weakening, *Geophys. Res. Lett.*, 44, 10592–10600, <https://doi.org/10.1002/2017GL075678>, 2017.
- Zhao, M., Cao, L., Bala, G., and Duan, L.: Climate Response to Latitudinal and Altitudinal Distribution of Stratospheric Sulfate Aerosols, *J. Geophys. Res.-Atmos.*, 126, e2021JD035379, <https://doi.org/10.1029/2021JD035379>, 2021.
- Zhou, C., Wang, M., Zelinka, M. D., Liu, Y., Dong, Y., and Armour, K. C.: Explaining Forcing Efficacy With Pattern Effect and State Dependence, *Geophys. Res. Lett.*, 50, e2022GL101700, <https://doi.org/10.1029/2022GL101700>, 2023.